iScience

CellPress
OPEN ACCESS

Article

Inhibition of the LRRC8A channel promotes microglia/macrophage phagocytosis and improves outcomes after intracerebral hemorrhagic stroke

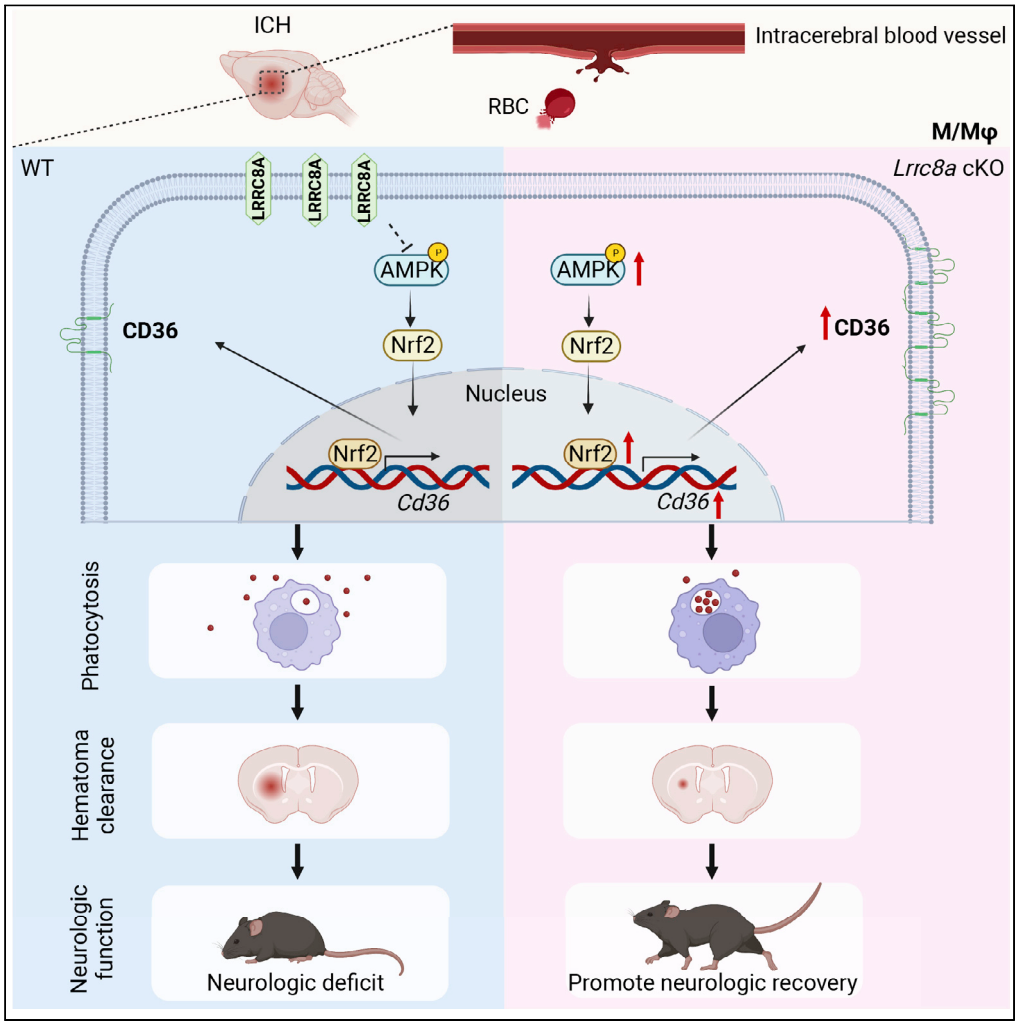

Jing Liu, Danmin Shen, Chao Wei, ..., Meng Xu, Fei Yang, Qian Li

drxm301@163.com (M.X.)
feiyang@ccmu.edu.cn (F.Y.)
qianli@ccmu.edu.cn (Q.L.)

Highlights

ICH upregulates the expression of LRRC8A on M/Mφ

Lrrc8a cKO in M/Mφ or blocking LRRC8A channel improves functional recovery in ICH

Dysfunction of the LRRC8A channel enhances M/Mφ phagocytosis in ICH

LRRC8A modulates the AMPK-Nrf2-CD36 axis under the stimulation of ICH

Liu et al., iScience *25*, 105527
December 22, 2022
https://doi.org/10.1016/j.isci.2022.105527

iScience

CellPress
OPEN ACCESS

Article

Inhibition of the LRRC8A channel promotes microglia/macrophage phagocytosis and improves outcomes after intracerebral hemorrhagic stroke

Jing Liu,[1,9] Danmin Shen,[2,9] Chao Wei,[1] Weihua Wu,[2] Zhaoli Luo,[2] Liye Hu,[2] Zhongnan Xiao,[2] Tingting Hu,[1] Qingyu Sun,[1] Xiaotong Wang,[1] Yumeng Ding,[1] Meng Liu,[1] Miaoyi Pang,[3] Kaiyuan Gai,[3] Yiran Ma,[3] Yichen Tian,[3] Yan Yu,[4] Peipei Wang,[1] Yun Guan,[5] Meng Xu,[6,*] Fei Yang,[1,7,*] and Qian Li[2,7,8,10,*]

SUMMARY

Promoting microglial/macrophage (M/Mφ) phagocytosis accelerates hematoma clearance and improves the prognosis of intracerebral hemorrhagic stroke (ICH). Cation channels such as Piezo1 modulate bacterial clearance by regulating M/Mφ. Whether LRRC8A, an anion channel, affects M/Mφ erythrophagocytosis and functional recovery after ICH was investigated here. We found that LRRC8A is highly expressed on M/Mφ in the perihematomal region of ICH mice. Conditional knockout of *Lrrc8a* in M/Mφ or treatment with an LRRC8A channel blocker accelerated hematoma clearance, reduced neuronal death, and improved functional recovery after ICH. Mechanistically, the LRRC8A channel inhibition promoted M/Mφ phagocytosis by activating AMP-activated protein kinase (AMPK), thereby inducing nuclear translocation of nuclear factor-erythroid 2 related factor 2 (Nrf2) and increasing *Cd36* transcription. Our findings illuminate the regulation of M/Mφ phagocytosis by the LRRC8A channel via the AMPK-Nrf2-CD36 pathway after ICH, suggesting that LRRC8A is a potential target for hematoma clearance in ICH treatment.

INTRODUCTION

The incidence of intracerebral hemorrhage (ICH) has increased by 47% over the past 20 years, becoming the most lethal subtype of stroke.[1] Clinical evidence indicates that the size and expansion of hematoma are the most important risk factors related to prognosis after ICH.[2] The leading causes of death and disability after ICH are the mass effects of hematoma and subsequent reactions to the toxic substances produced by its dissolution. Therefore, prompt removal of hematoma is vital to improving outcomes. Unfortunately, no treatment is available to accelerate the clearance and inhibit expansion of hematoma.[3]

Resident-activated microglia and infiltrating monocytes/macrophages (M/Mφ) respond quickly to brain damage, and play crucial roles in clearing the hematoma and preventing red blood cell (RBC)-induced neuronal cytotoxicity after ICH.[4] The enhancement of M/Mφ erythrophagocytosis promotes hematoma resolution, limits brain inflammation, reduces neuronal damage, and improves long-term neurologic functional recovery after ICH.[5] M/Mφ possess a phagocytosis-related receptor called CD36 that is transcribed mainly by peroxisome proliferator-activated receptor gamma and regulated by interleukin (IL)-10, Wogonin, and the Gas6-AXL axis.[6–11] How different ion channels regulate erythrophagocytosis and CD36 in M/Mφ remains largely unexplored.

The LRRC8A channel is an anion channel widely expressed in mammalian cells. It is encoded by *Lrrc8a–e*, but *Lrrc8a* encodes the essential subunit that regulates channel activity.[12,13] Functionally, LRRC8A increases permeability of cells to the swelling-activated efflux of Cl^- and regulates cell volume.[14] It is also involved in the pathophysiologic processes of several central nervous system diseases.[15–18] Importantly, a loss of LRRC8A in astrocytes or neurons decreases the release of glutamate and alleviates brain injury in ischemic stroke.[19,20] Whereas loss of the microglial LRRC8A channel did not affect microglial morphology nor the extent of brain damage.[21] In the peripheral system, the macrophagic LRRC8A channel participates in the hypotonicity-induced NLRP3 inflammasome activation and the process of pyroptotic cell swelling.[22] However, our knowledge of the expression and function of the LRRC8A channel in ICH, which is

[1]Department of Neurobiology, School of Basic Medical Sciences, Capital Medical University, Beijing 100069, China

[2]Department of Biochemistry and Molecular Biology, School of Basic Medical Sciences, Capital Medical University, Beijing 100069, China

[3]School of Basic Medical Sciences, Capital Medical University, Beijing 100069, China

[4]Chinese Institute of Rehabilitation Science, China Rehabilitation Research Center, Beijing Key Laboratory of Neural Injury and Rehabilitation, Beijing 100068, China

[5]Department of Anesthesiology and Critical Care Medicine, the Johns Hopkins University, School of Medicine, Baltimore, MD 21205, USA

[6]Department of Musculoskeletal Tumor, Senior Department of Orthopedics, the Fourth Medical Center of PLA General Hospital, Beijing 100142, China

[7]Advanced Innovation Center for Human Brain Protection, Beijing Key Laboratory of Neural Regeneration and Repair, Capital Medical University, Beijing 100069, China

[8]Key Laboratory of Cancer Invasion and Metastasis Research, Capital Medical University, Beijing, China

[9]These authors contributed equally

[10]Lead contact

*Correspondence: drxm301@163.com (M.X.), feiyang@ccmu.edu.cn (F.Y.), qianli@ccmu.edu.cn (Q.L.)

https://doi.org/10.1016/j.isci.2022.105527

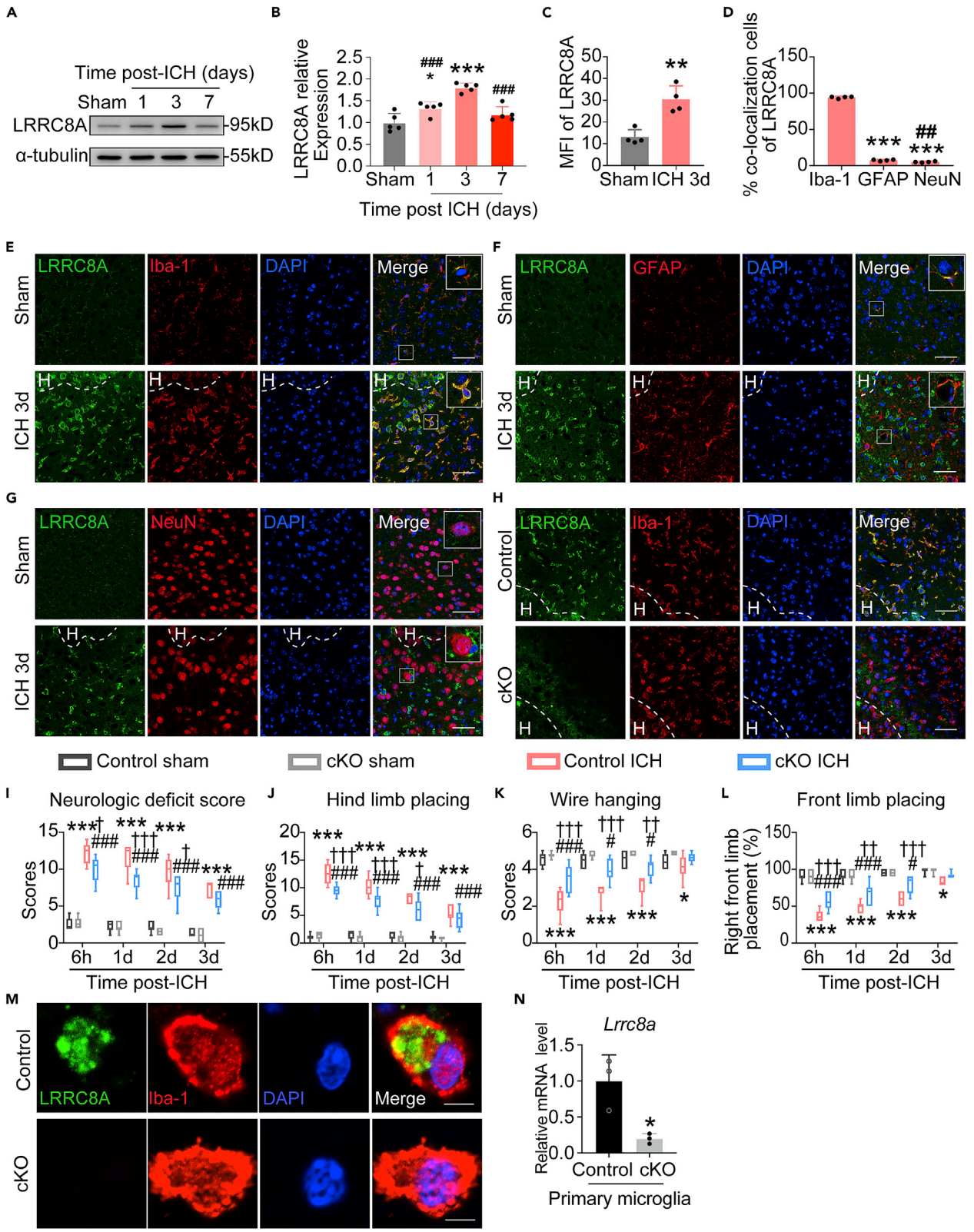
A
Time post-ICH (days)
Sham 1 3 7
LRRC8A
95kD
α-tubulin
55kD
B
LRRC8A relative Expression
Sham 1 3 7
Time post ICH (days)
C
MFI of LRRC8A
Sham ICH 3d
D
% co-localization cells of LRRC8A
Iba-1 GFAP NeuN
E
Sham
ICH 3d
LRRC8A
Iba-1
DAPI
Merge
F
GFAP
G
NeuN
H
Control
cKO
Control sham
cKO sham
Control ICH
cKO ICH
I
Neurologic deficit score
Scores
6h 1d 2d 3d
Time post-ICH
J
Hind limb placing
K
Wire hanging
L
Front limb placing
Right front limb placement (%)
M
N
Lrrc8a
Relative mRNA level
Control cKO
Primary microglia

Figure 1. LRRC8A is upregulated in M/Mφ in the perihematomal region after ICH and affects prognosis

(A–D) Male C57BL/6 mice (6–8 weeks) underwent autologous intrastriatal blood injection or sham procedure. Proteins were extracted from the ipsilateral striatum.

(A) Representative images of western blot.

(B) Quantifications of LRRC8A level in each group. α-tubulin served as an internal control.

(C) The mean fluorescence intensity (MFI) of LRRC8A immunoreactivity.

(D) Percentages of $Iba1^+LRRC8A^+$, $GFAP^+LRRC8A^+$, and $NeuN^+LRRC8A^+$ in $LRRC8A^+$ cells in the perihematomal region of each group. Data are presented as mean ± SD.

(E–G) Representative images show the perihematomal region of brain sections stained with antibodies to LRRC8A and Iba-1 (E), GFAP (F), or NeuN (G) at day 3 post-ICH. The nuclei were stained with DAPI. The dashed line indicates hematoma core; H: hematoma.

(H) Male C57BL/6 tamoxifen injected (control) mice and *Lrrc8a*$^{fl/fl}$; *Cx3cr1*$^{creERT/+}$ (*Lrrc8a* cKO) mice (6–8 weeks) underwent intrastriatal injection with autologous blood or sham procedure. Brain sections were stained with LRRC8A and Iba-1 antibodies at day 3 post-ICH. Nuclei were stained with DAPI.

(I–L) Mice were evaluated by neurologic deficit score (I), hind limb placing test (J), wire hanging test (K), and right front limb placing test (L). (M, N) Primary microglia cultured from control or cKO mice (6–8 weeks).

(M) Immunofluorescence immunostaining was performed using LRRC8A and Iba-1 antibodies. Representative images show the LRRC8A expression of each group.

(N) Real-time RT-PCR was performed to detect mRNA levels of *Lrrc8a* of each group. GAPDH served as an internal control. Results are presented as box and whisker plots (min to max). B, D: One-way ANOVA with Tukey's multiple-comparison test; C, N: Student's *t* test followed by Welch's correction; i-l: two-way ANOVA with Tukey's multiple-comparison test. *p< 0.05, **p< 0.01, ***p< 0.001 vs. sham (B, C), Iba-1 (D), control (N), or corresponding control sham (I-L); #p< 0.05, ##p< 0.01, ###p< 0.001 vs. ICH day-3 (B), GFAP (D), or corresponding cKO sham (I-L); †p< 0.05, ††p< 0.01, †††p< 0.001 vs. corresponding control ICH. Each group contained 5 (B, C), 4 (D), 6 (I-L) animals, or 3 (N) times independently. Results are from at least three independent experiments. Scale bars: 50 μm (E–H), 5 μm (M).

a more lethal stroke subtype where M/Mφ plays a vital role in its progression by accelerating hematoma clearance and modulating inflammation, is limited. Accordingly, we investigated whether the LRRC8A channel affects M/Mφ erythrophagocytosis, hematoma clearance, and functional outcome in mice after ICH, and explored the underlying mechanisms.

This current study shows that ICH triggers the upregulation of LRRC8A expression on M/Mφ. Conditional knockout of *Lrrc8a* in M/Mφ or pharmaceutical blocking of the LRRC8A channel accelerates hematoma resolution and improves functional recovery after ICH. We also identified the dysfunction of the LRRC8A channel enhances M/Mφ phagocytosis *via* modulating the AMPK-Nrf2-CD36 axis under the stimulation of hemin. Our findings suggest that targeting the LRRC8A channel may represent a potential therapeutic strategy for ICH by regulating M/Mφ erythrophagocytosis.

RESULTS

LRRC8A expression is upregulated in M/Mφ in the perihematomal region and affects prognosis after ICH

We first examined the expression of LRRC8A at different time points after intrastriatal injection of autologous blood to induce ICH in wildtype mice. Western blot analysis showed that LRRC8A protein level in the ipsilateral striatum was markedly increased and peaked at day 3 after ICH (Figures 1A and 1B). LRRC8A immunoreactivity also was significantly increased in the perihematomal region of the striatum at day 3 post-ICH (Figure 1C). Moreover, LRRC8A immunoreactivity was highly colocalized with Iba-1 (a specific M/Mφ marker; Figures 1D and 1E). In contrast, few activated astrocytes (labeled with GFAP) and neurons (labeled with NeuN) in this region expressed LRRC8A (Figures 1F and 1G). Of note, LRRC8A was expressed in astrocytes adjoining blood vessels (Figure S1A) and in cortical neurons (Figure S1B).

To explore the functional roles of LRRC8A on M/Mφ in ICH, we developed conditional knock out (cKO) mice by crossing *Lrrc8a*$^{fl/fl}$ and *Cx3cr1*$^{creERT/+}$ mouse strains (Figures S2A and S2B). *Lrrc8a* was selectively deleted in M/Mφ of adult cKO mice by injecting tamoxifen (referred to as LRRC8A cKO). The majority of reactive M/Mφ ($Iba\text{-}1^+$) were $LRRC8A^+$ after ICH in age-matched male control mice. In contrast, very few LRRC8A and Iba-1 double-stained cells were present in LRRC8A cKO mice (Figure 1H). Importantly, LRRC8A cKO mice exhibited significantly greater improvements in neurologic and motor functions after ICH than did control mice, as suggested by the lower neurological deficit score and better performance in the hindlimb placement, wire hanging, and front limb placement tests (Figures 1I–1L). In addition, LRRC8A cKO mice showed better neurologic and motor function recovery in the collagenase-induced ICH model (Figures S2C–S2F). We further extracted mouse primary microglia from the cKO and control mouse brain, and found that the protein (Figure 1M) and mRNA (Figure 1N) levels of *Lrrc8a* were barely detectable in cKO microglia. These data indicate that the aggravated neurobehavior was because of the deficiency of *Lrrc8a* in M/Mφ.

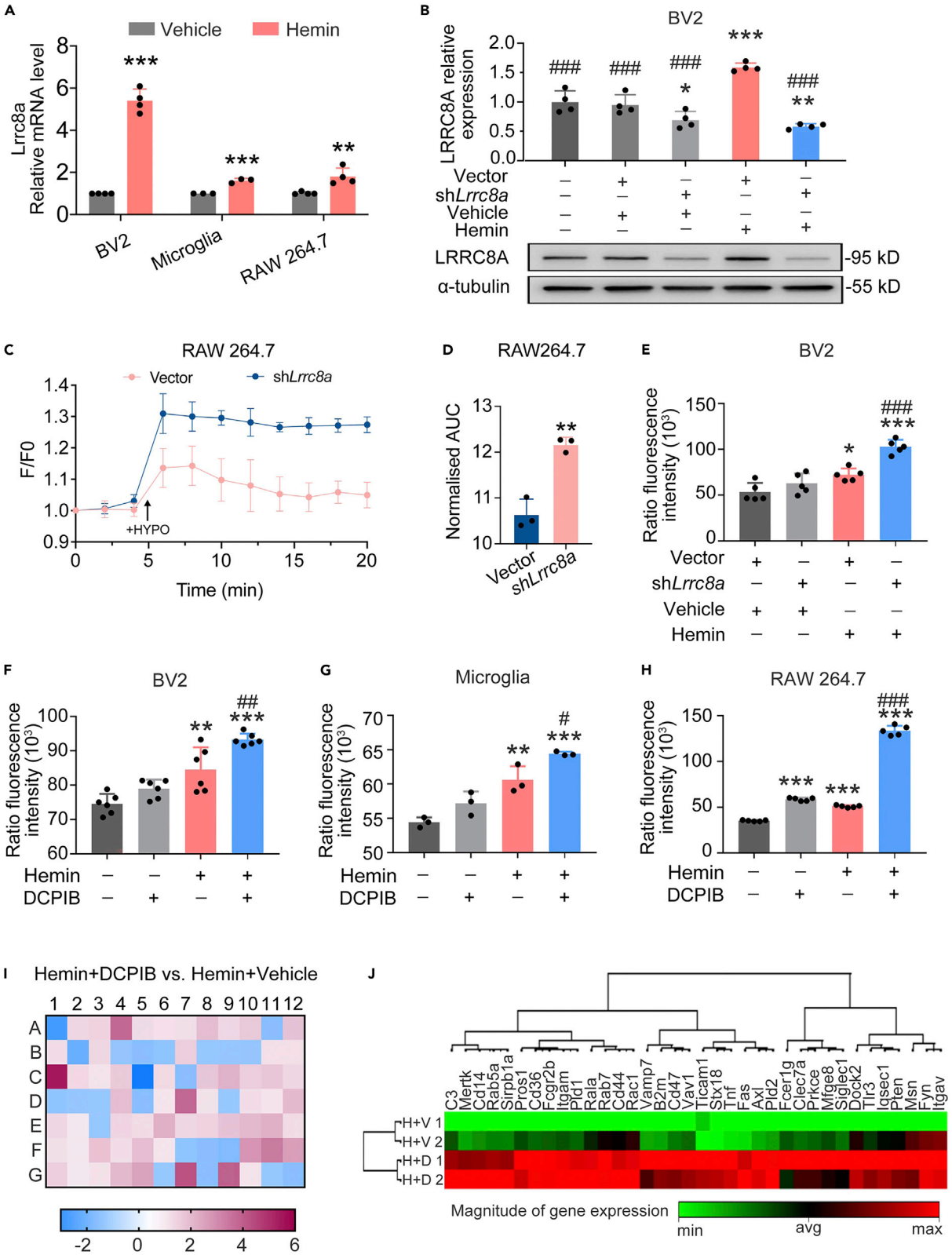
A
Vehicle
Hemin
Lrrc8a
Relative mRNA level
BV2
Microglia
RAW 264.7
B
BV2
LRRC8A relative expression
Vector
shLrrc8a
Vehicle
Hemin
LRRC8A
α-tubulin
-95 kD
-55 kD
C
RAW 264.7
Vector
shLrrc8a
F/F0
+HYPO
Time (min)
D
RAW264.7
Normalised AUC
Vector
shLrrc8a
E
BV2
Ratio fluorescence intensity (10³)
Vector
shLrrc8a
Vehicle
Hemin
F
BV2
Ratio fluorescence intensity (10³)
Hemin
DCPIB
G
Microglia
Ratio fluorescence intensity (10³)
Hemin
DCPIB
H
RAW 264.7
Ratio fluorescence intensity (10³)
Hemin
DCPIB
I
Hemin+DCPIB vs. Hemin+Vehicle
J
C3
Mertk
Cd14
Rab5a
Sirpb1a
Pros1
Cd36
Fcgr2b
Itgam
Pld1
Rala
Rab7
Cd44
Rac1
Vamp7
B2m
Cd47
Vav1
Ticam1
Stx18
Tnf
Fas
Axl
Pld2
Fcer1g
Clec7a
Prkce
Mfge8
Siglec1
Dock2
Tlr3
Iqsec1
Pten
Msn
Fyn
Itgav
H+V 1
H+V 2
H+D 1
H+D 2
Magnitude of gene expression
min
avg
max

Figure 2. Genetic and pharmacologic suppression of LRRC8A facilitates phagocytosis by M/Mφ *in vitro*

(A) BV2 cells, mouse primary microglia, or RAW 264.7 cells were exposed to hemin or vehicle for 6 h. RT-qPCR was performed to detect mRNA levels of *Lrrc8a* in each cell type. *GAPDH* served as an internal control.

(B) BV2 cells were transfected with *Lrrc8a* shRNA lentiviruses or scrambled shRNA (vector) and then incubated with hemin or vehicle for 6 h. Representative western blot images and quantification of LRRC8A protein levels in each group are shown. α-tubulin served as an internal control.

(C and D) LRRC8A was knocked down using lentivirus *Lrrc8a* shRNA, vector shRNA as the control in RAW 264.7 cells which were further exposed to the hypotonic solution.

(C) Calcein fluorescence detection of control and sh*Lrrc8a* in RAW 264.7 cells exposed to the hypotonic solution.

(D) Quantification of the area under curve.

(E) Cells were incubated with fluorescence-conjugated latex beads for 20 min, and the fluorescence intensities of the engulfed beads were quantified.

(F–H) BV2 cells (F), primary microglia (G), and RAW 264.7 cells (H) were exposed to hemin + vehicle or hemin + DCPIB for 6 h, and the fluorescence intensities of the engulfed beads in each cell type were quantified.

(I and J) Heatmap showing differential expression of 84 phagocytic genes in BV2 cells treated with hemin + DCPIB as compared to that in BV2 cells treated with hemin + vehicle. RT^2 Profiler PCR Array Mouse Phagocytosis was used (I). Phagocytic genes with a tendency toward increased expression are presented as a clustergram (J). A-F: Data are presented as mean ± SD. A, D: Student's *t* test followed by Welch's correction; B, C, E-H: one-way ANOVA with Tukey's multiple-comparison test. *p< 0.05, **p< 0.01, ***p< 0.001 vs. vehicle (A, F-H) or vector + vehicle (B, E); #p< 0.05, ##p< 0.01, ###p< 0.001 vs. hemin (F-H) or vector + hemin (B, E). Each experiment was repeated 3 (A, C, D, G), 4 (A, B), 5 (E, H), or 6 (F) times independently.

Knockdown of *Lrrc8a* in striatal astrocytes and neurons does not influence ICH outcomes

Astrocytic and neuronal LRRC8A affect ischemic stroke prognosis.[19,20] Although the expression level of LRRC8A was relatively low in astrocytes and neurons in perihematomal region in WT mice after ICH (Figures 1F and 1G), we further examined whether knocking down *Lrrc8a* in these cells affects ICH outcomes. Compared to astrocytes and neurons, the rate of M/Mφ infection by AAV is very low.[23,24] Therefore, stereotactical injection of pAAV 9-cytomegalovirus (CMV)-mCherry-*Lrrc8a* shRNA into the ipsilateral striatum predominantly suppressed *Lrrc8a* expression in neurons and astrocytes, but not in M/Mφ in the perihematomal region at day 3 post-ICH (Figures S3A and S3B). However, knocking down both neuronal and astrocytic LRRC8A did not improve the neurologic and motor dysfunctions after ICH, as compared to scrambled shRNA treatment (Figures S3C–S3F). To further confirm the knockdown efficiency of *Lrrc8a*, we investigated the expression levels of *Lrrc8a*. Injection of *Lrrc8a* shRNA into the ipsilateral striatum significantly decreased the mRNA level (Figure S3G) and protein levels of *Lrrc8a* (Figures S3H and S3I) at 3 days post-ICH. Collectively, these findings suggest that LRRC8A expressed on M/Mφ is important to the prognosis after ICH.

Suppression of LRRC8A enhances M/Mφ phagocytosis

Effective phagocytosis of erythrocytes by M/Mφ is important to limiting iron overload-induced neuronal toxicity and thereby improving prognosis of ICH. We cultured the microglial cell line BV2, the mouse primary microglia, and macrophage cell line RAW 264.7, and directly examined whether LRRC8A mediates the phagocytosis of RBCs by M/Mφ. Hemin is a degradative product of RBCs and has been commonly used to mimic ICH toxicity. Hemin significantly upregulated the mRNA level of *Lrrc8a* in phagocytes (Figure 2A). We next knocked down *Lrrc8a* by infecting BV2 cells with *Lrrc8a* shRNA lentiviruses (Figure 2B). To confirm the effect of VRAC function of M/Mφ after depletion of LRRC8A, we knocked down the *Lrrc8a* in RAW 264.7 cells with lentivirus and observed the temporal dynamics of cell volume fluctuations by hypotonic induction. With exposure to 30% hypotonic solution, control cells rapidly developed regulatory volume decrease (RVD) and cell volume largely returned to basal levels within 15 min based on the calcein fluorescence intensity. In contrast, *Lrrc8a* shRNA cells showed a significant absence of RVD functional response (Figures 2C and 2D), which pointed out that deficiency of *Lrrc8a* adequately responds to the VRAC dysfunction.

We then incubated cells with fluorescence-conjugated latex beads for the phagocytosis assay. Hemin increased phagocytic ability, as compared to that in the vehicle group and genetic silencing of *Lrrc8a* significantly promoted phagocytosis of the beads (Figure 2E). We further confirmed M/Mφ phagocytosis by pharmacologic inhibition of the LRRC8A channel with DCPIB. The dosage of DCPIB (20 μM) was selected according to recent studies.[25,26] The cell viability was not impacted by 20 μM DCPIB and 6 h of treatment through our observation under the microscope during the experiment (not shown). Consistent with these above findings, DCPIB enhanced M/Mφ phagocytosis only when co-treatment with hemin (Figures 2F–2H).

To further examine the role of LRRC8A in M/Mφ phagocytosis and its downstream targets, we used a mouse phagocytic PCR array to detect the affected phagocytic genes. Compared with hemin treatment alone, co-administration of DCPIB and hemin boosted the expression of most phagocytic genes in this panel (Figures 2I and 2J and Table S1).

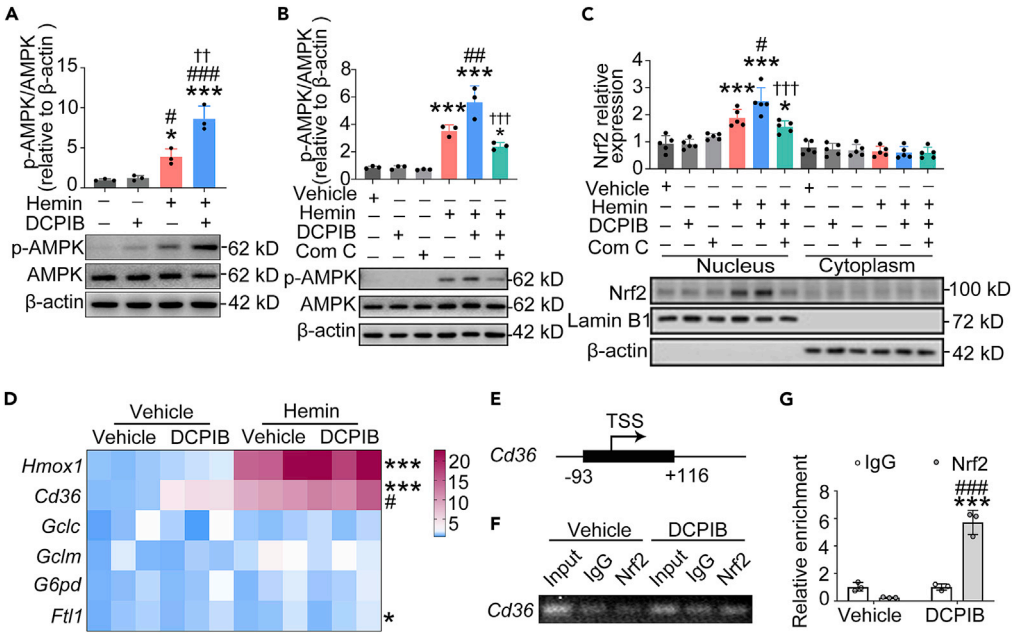

Figure 3. Pharmacologic inhibition of LRRC8A activates AMPK-Nrf2 axis in BV2 cells

(A–C) Representative western blot images and quantification of pAMPK/AMPK (A, B) and Nrf2 (C) protein levels in BV2 cells after indicated drug treatments. β-actin served as an internal control.

(D) Heat map shows RT-qPCR–determined mRNA levels of *Hmox1*, *Cd36*, *Gclc*, *Gclm*, *G6pd*, and *Ftl1* in BV2 cells after drug treatment. *GAPDH* served as an internal control.

(E) Diagram shows the design of initial primer sets for the ChIP assay.

(F) Lysates from BV2 cells were extracted to ChIP by anti-Nrf2 antibody (Nrf2). Sonicated chromatin was used as input DNA control (input). IgG was used as random control IgG. The band of ChIP-PCR products amplified by *Cd36* primer is shown.

(G) Immunoprecipitate was quantified by real-time PCR. Relative enrichment was normalized with input. Data are presented as mean ± SD. A-C: One-way ANOVA with Tukey's multiple-comparison test; D: Student's *t* test followed by Welch's correction; G: two-way ANOVA with Sidak's multiple-comparison test. *p< 0.05, **p< 0.01, ***p< 0.001 versus vehicle, IgG (G), or hemin + DCPIB versus hemin + vehicle (D); #p< 0.05, ##p< 0.01, ###p< 0.001 versus DCPIB (A-D) or vehicle (G); †p< 0.05, †††p< 0.001 vs. hemin + vehicle. Each experiment was repeated 3 (A, D, G) or 4 (B, C) times independently.

Blocking the LRRC8A channel activates AMPK-Nrf2-CD36 axis *in vitro*

AMP-activated protein kinase (AMPK), a heterotrimeric kinase, plays an important role in inflammation,[27] glucose homeostasis, metabolic regulation,[28] and mitochondrial biogenesis.[29] There is growing evidence that AMPK activation plays an essential role in phagocytosis.[30,31] Hereby, we investigated whether blocking the LRRC8A channel affects AMPK. Hemin activated AMPK by increasing AMPK phosphorylation (p-AMPK, Figure 3A), the levels of which were further increased by DCPIB. The upregulated p-AMPK level was reduced by the AMPK inhibitor Compound C (Figure 3B). The classic transcription factor nuclear factor-erythroid 2 related factor 2 (Nrf2) can be regulated by AMPK,[32] and plays a crucial role in phagocytosis as well as inflammatory and oxidative stress.[33–35] Hemin, but not vehicle, induced Nrf2 nuclear translocation, which was enhanced by DCPIB. This effect was reversed by p-AMPK inhibitor Compound C (Figure 3C).

We next examined the transcription levels of Nrf2 target genes, such as those that encode heme oxygenase-1 (HMOX-1), glutamate-cysteine ligase modifier (GCLM), glucose-6-phosphate dehydrogenase (G6PD), ferritin light chain (FTL), and CD36, which contains conserved antioxidant response elements.[36,37] The mRNA levels of *Hmox1* and *Cd36* were increased by hemin, and further upregulated by the addition of DCPIB (Figure 3D). HMOX-1 is the key enzyme involved in hemin degradation and showed positive feedback to intracellular hemin concentration.

Because CD36 is one of the most important phagocytosis-related receptors,[7,38–40] we focused on it in subsequent studies. Nrf2 activator upregulated CD36 expression in monocytes.[41] Yet, it remains unclear

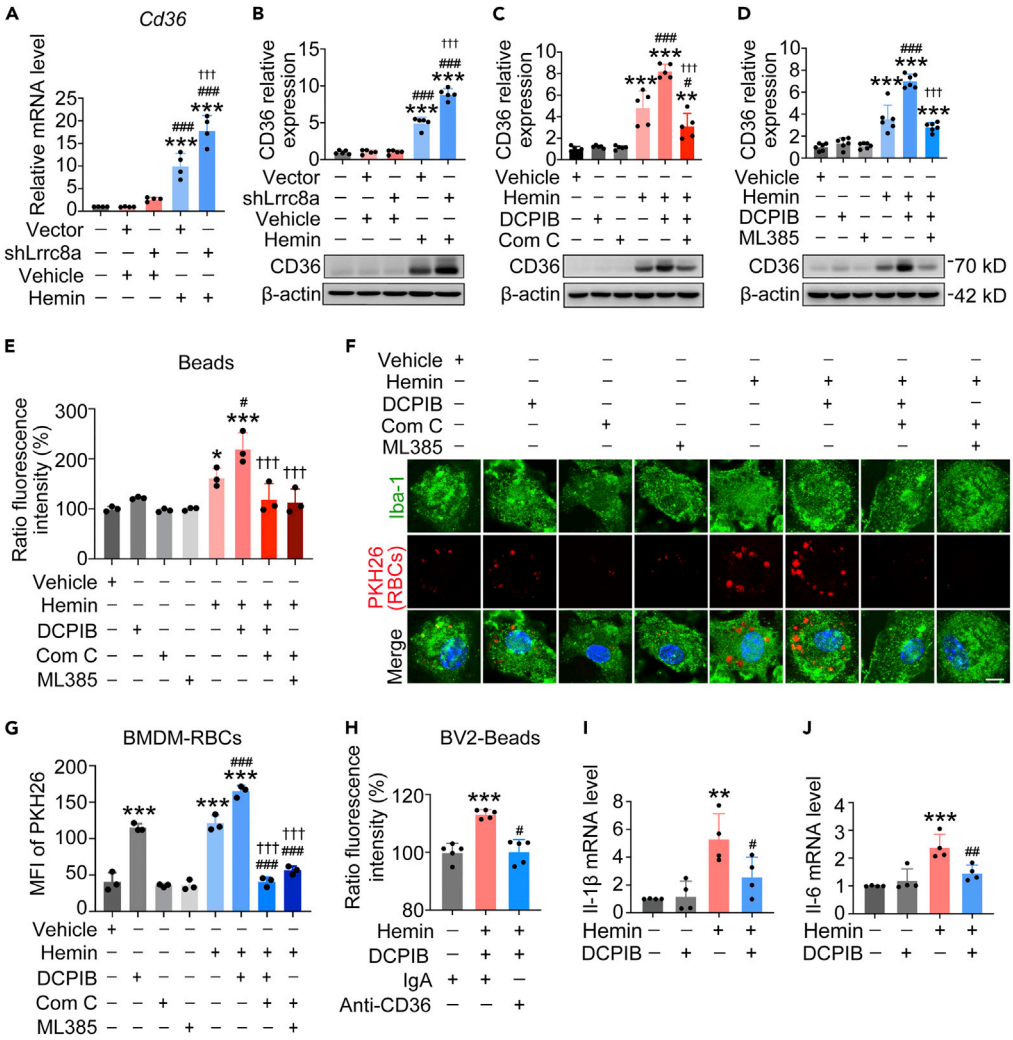

Figure 4. Inhibition of LRRC8A in M/Mφ upregulates CD36 expression by activating the AMPK-Nrf2 axis in BV2 cells

(A and B) The mRNA (A) and protein (B) levels of CD36 in BV2 cells infected with *Lrrc8a* shRNA or vector lentiviruses, and incubated with hemin or vehicle (DMSO) for 6 h.

(C and D) CD36 protein levels in BV2 cells at 6 h after drug or vehicle treatment.

(E) BV2 cells were treated as indicated and incubated with fluorescence-conjugated latex beads (4 μM) for 20 min; the fluorescence intensities of the engulfed beads in the cells were quantified.

(F) Representative images of bone marrow-derived macrophages (BMDMs) stained with Iba-1 antibody and red blood cells (RBCs) labeled with PKH26. The nuclei were stained with DAPI.

(G) Quantitative analysis of PKH26 after indicated treatments.

(H) Fluorescence intensities of engulfed beads in BV2 cells after 6 h exposure to the indicated drug treatments.

(I and J) mRNA levels of *Il-1β* (I) and *Il-6* (J). Data are presented as mean ± SD. A-E, G-J: One-way ANOVA with Tukey's multiple-comparison test. *p< 0.05, **p< 0.01, ***p< 0.001 versus vehicle/vector (A-E, G, I, J) or IgA (H); #p< 0.05, ##p< 0.01, ###p< 0.001 vs. *Lrrc8a* shRNA + vehicle (A, B), hemin + vehicle (C-E, G), hemin + DCPIB + IgA (H), or hemin + DCPIB (I, J); †††p< 0.001 vs. vector + hemin (A, B), or hemin + DCPIB (C-E, G). Each experiment was repeated 3 (E, G), 4 (A), 5 (B, H), or 6 (C, D) times independently, and each group contained 4 animals (I).

whether Nrf2 directly binds to the promoter region of *Cd36*. Our chromatin immunoprecipitation (ChIP) assay showed that DCPIB induced binding of Nrf2 to the promoter region of *Cd36* (Figures 3E–3G). In addition, both DCPIB and *Lrrc8a* knockdown significantly upregulated the mRNA and protein levels of *Cd36* (Figures 4A–4D). Importantly, the increased CD36 expression after co-treatment with DCPIB and hemin was blocked by p-AMPK inhibitor Compound C (Figure 4C), and also by Nrf2 inhibitor ML385 (Figure 4D).

To further determine whether LRRC8A affects M/Mφ phagocytosis by regulating the AMPK-Nrf2-CD36 axis, we incubated BV2 cells with either fluorescence-conjugated latex beads (Figure 4E) or RBCs labeled with lipophilic fluorescent dye PKH26 (Figures 4F and 4G). The increased phagocytotic ability produced by hemin and DCPIB co-treatment was attenuated by Compound C and ML385 (Figures 4E–4G) and was reversed by CD36-neutralizing antibodies (Figure 4H).

Sustained activation of M/Mφ may increase the expression of proinflammatory mediators, which can induce neuronal death. Proinflammatory cytokines are mainly expressed by reactive microglia in the brain. Our real-time PCR data revealed that *Il-1β* and *Il-6* were upregulated in hemin-treated BV2 cells, but that the upregulation was significantly reduced by DCPIB (Figures 4I and 4J). Collectively, these results indicate that the LRRC8A channel dysfunction or inhibition may induce cellular stress, which in turn activates the AMPK-Nrf2 axis to upregulate *Cd36* expression and promote M/Mφ phagocytosis after ICH.

Inhibition of LRRC8A channel accelerates hematoma clearance via AMPK-Nrf2-CD36 axis *in vivo*

To test whether LRRC8A inhibition also affects CD36 expression *in vivo*, we induced ICH in LRRC8A cKO mice. Compared to control mice, cKO mice showed a profound upregulation of CD36 protein level after ICH that was attenuated by intracerebroventricular injection of AMPK and Nrf2 inhibitors (Figure 5A). Importantly, cKO mice exhibited a much smaller hematoma volume than control mice after ICH. This outcome was also reversed in cKO mice by administration of p-AMPK inhibitor (Figures 5B and 5C), Nrf2 inhibitor (Figures 5B and 5C), and CD36-neutralizing antibodies (Figures 5D and 5E). Because the initial bleeding volumes were similar in cKO and control mice (i.e., the same amount of blood was injected into the striatum to induce ICH), our findings suggest that knocking out of *Lrrc8a* selectively in M/Mφ accelerated hematoma clearance *in vivo* after ICH.

After ICH, the direct mechanical effects of hematoma lead to primary brain injury. The development of perihematomal edema leads to secondary brain injury caused by the disruption of blood-brain barrier (BBB) integrity and adjacent tissue injury.[42] Moreover, we examined changes in mRNA and protein levels of CD36 after pharmacologically blocking the LRRC8A channel in WT mice after ICH. Consistent with findings in cKO mice, DCPIB increased CD36 expression (Figures 5F and 5G) and dose-dependently accelerated hematoma clearance in both autologous blood-injected (Figures 5H–5J) and collagenase-injected (Figures S4A–S4C) ICH models, as indicated by reduced hematoma volume and hemoglobin content.

DCPIB reduces neuronal loss and improves functional outcomes after ICH

Accelerating hematoma clearance after ICH may eventually reduce neuronal damage. Indeed, DCPIB decreased the number of Fluoro-Jade C $(FJC)^+$ degenerating neurons (Figures 6A and 6B), and increased the number of cresyl violet $(CV)^+$ surviving neurons in the perihematomal region after ICH (Figures 6C and 6D). Moreover, the lesion volume was also dose-dependently reduced by DCPIB (Figures 6E and 6F). The attenuated neuronal death and lesion volume ultimately translated into improved neurologic and motor function in ICH mice. In both autologous blood-injected (Figures 6G–6J) and collagenase-injected (Figures S5A–S5D) ICH models, DCPIB-treated mice had lower neurological deficit scores (Figures 6G and S5A) and exhibited better performance in the hindlimb placing test (Figures 6H and S5B), wire hanging test (Figures 6I and S5C), and front limb placing test (Figures 6J and S5D) than did the vehicle-treated group.

DISCUSSION

Clinical evidence has shown that hematoma volume is positively correlated with the levels of hemoglobin content, neurotoxic factors, and mortality after ICH and negatively correlated with favorable prognosis and functional recovery.[43,44] An international multicenter randomized clinical trial, MISTIE III (minimally invasive surgery plus rt-PA), suggested that increasing hematoma clearance ameliorates the mortality rate in ICH patients.[45] Notably, at 1-year post-ICH onset, the neurologic deficits were improved only in patients with a residual hematoma volume less than 15 mL.[45,46] Therefore, leveraging endogenous mechanisms of RBC phagocytosis may help reduce hematoma volume and improve functional recovery.

Activated resident microglia and infiltrating monocytes/macrophages (M/Mφ) mediate hematoma clearance after ICH. M/Mφ can be quickly (in seconds) recruited to the perihematomal region after bleeding. This M/Mφ activation peaks at day 3 after ICH and persists for several weeks.[47,48] Changes in LRRC8A

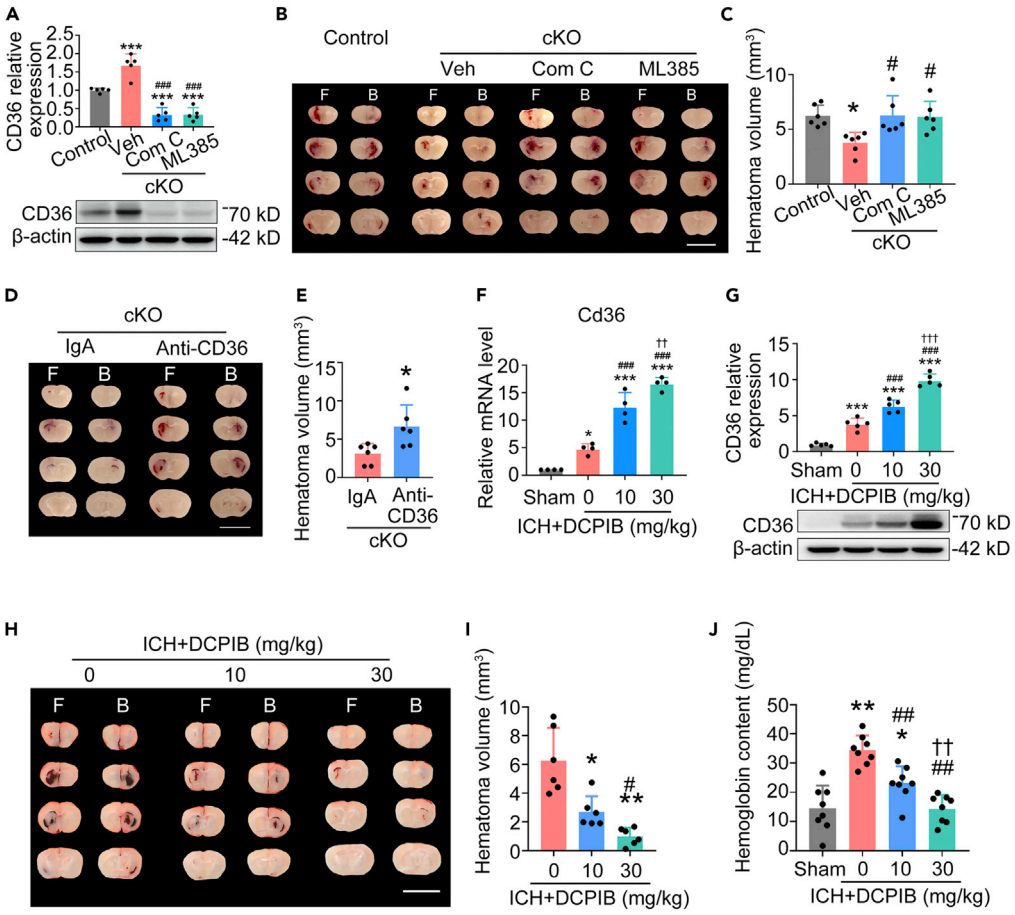

Figure 5. CD36 is the downstream effector of LRRC8A suppression that accelerates hematoma clearance after ICH *in vivo*

(A) Representative Western blot images and quantification of CD36 protein levels in tamoxifen injected (control) C57BL/6 mice and *Lrrc8a*$^{fl/fl}$; *Cx3cr1*$^{creERT/+}$ (*Lrrc8a* cKO) mice (male, 6–8 weeks) that were injected with autologous blood and treated with the indicated drugs.

(B and C) Representative images (B) and quantification of hematoma volume (C) on day 3 post-ICH.

(D and E) Representative images (D) and quantification of hematoma volume (E) on day 3 post-ICH in *Lrrc8a* cKO mice that received anti-CD36 antibody or control (IgA) treatment.

(F) mRNA levels of CD36 in male WT mice (6–8 weeks) that underwent sham procedure or autologous blood injection followed by DCPIB treatment. Different dosages of DCPIB were administered once daily (*i.p.*) until sacrifice. Proteins were extracted from the ipsilateral striatum.

(G) Representative western blot images and quantification of CD36 protein level in each group.

(H–J) Representative images of hematoma in serial coronal brain sections (H) and quantification of hematoma volume (I) and hemoglobin content (J) on day 3 post-ICH after DCPIB treatment. Data are presented as mean ± SD. A, C, F, G, I, J: One-way ANOVA with Tukey's multiple-comparison test; E: Student's *t* test followed by Welch's correction. *p< 0.05, **p< 0.01, ***p< 0.001 vs. control + ICH (A, C), cKO + ICH + IgA (E), ICH + DCPIB (0 mg/kg) (F, G, I), or sham (J); #p< 0.05, ##p< 0.01, ###p< 0.001 vs. cKO + ICH + vehicle (A, C), ICH + DCPIB (10 mg/kg) (F, G, I), or ICH + DCPIB (0 mg/kg) (J); ††p< 0.01 vs. ICH + DCPIB (10 mg/kg) (F, G, J). Each group contained 6 (I) or 8 (J) animals. Scale bars: 1 cm (B, D, H).

expression matched the time course of M/Mφ activation after ICH, and LRRC8A immunoreactivity highly colocalized with M/Mφ in the perihematomal region. These findings support the notion that the LRRC8A channel activation is involved in the engulfment of RBCs and the production of inflammatory factors by M/Mφ.

Although previous studies showed an increase in cell volume of the activated or phagocytotic M/Mφ, it was unclear whether volume changes affect M/Mφ function. Dysfunction of the LRRC8A channel in macrophages are unable to undergo hypotonicity-induced regulatory volume decrease (RVD) and keeps cell

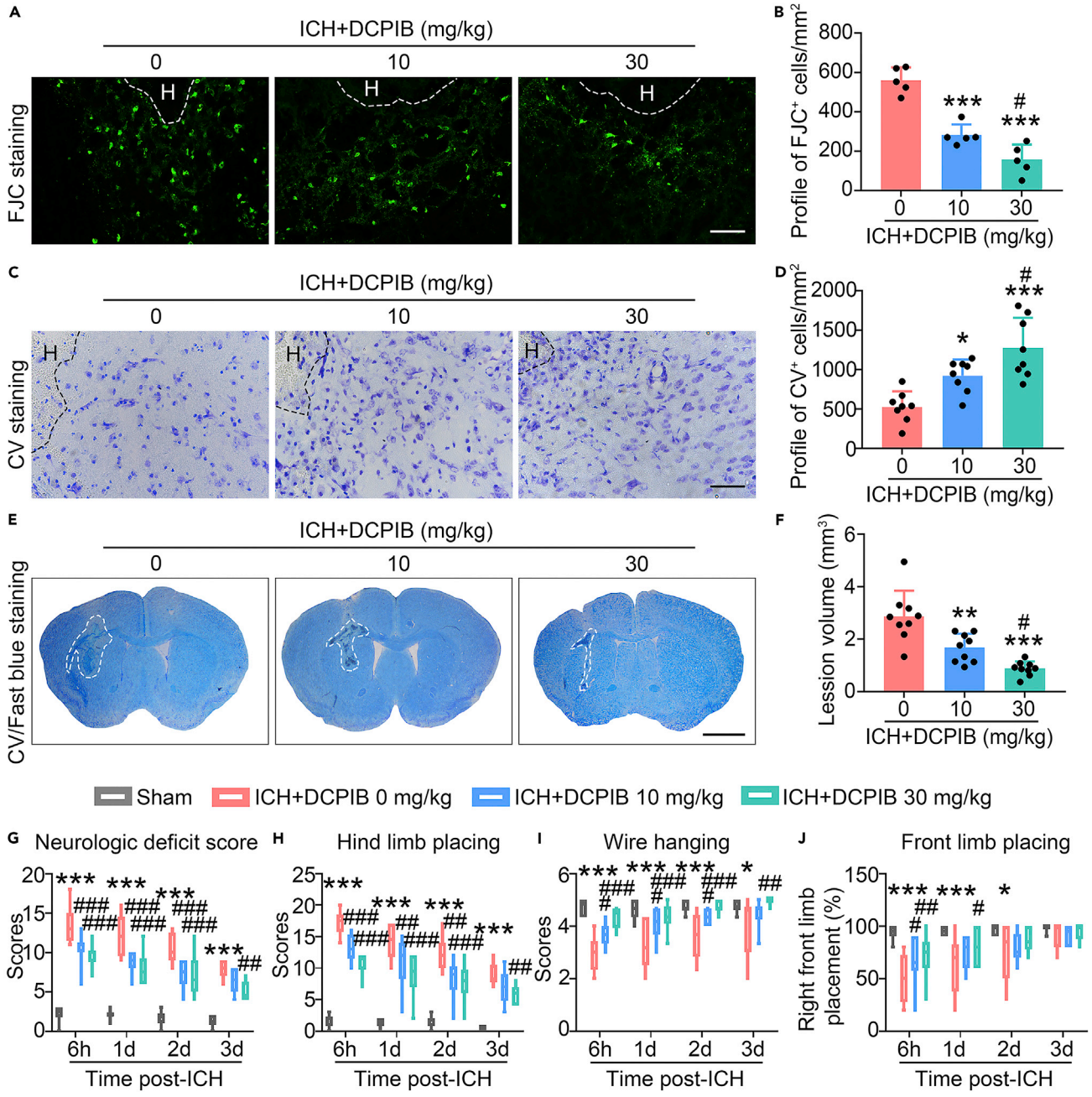

Figure 6. Pharmacologic inhibition of LRRC8A reduces neuronal loss and improves neurologic function after ICH

Male C57BL/6 mice (6–8 weeks) underwent autologous blood injection or sham procedure. Different doses of DCPIB were administered (*i.p.*) once daily until sacrifice.

(A) Representative images of Fluoro-Jade C (FJC)–stained brain sections.

(B) Quantification of FJC-positive neurons.

(C) Representative images of brain sections stained with cresyl violet (CV).

(D) Quantification of CV-positive neurons.

(E) Representative images of brain sections stained with CV/Fast blue.

(F) Quantification of lesion volume. (A-F) Dashed line indicates hematoma core; (H) hematoma. Data are presented as mean ± SD.

(G–J) Changes in neurological deficit score (G) and performance in the hind limb placing test (H), wire hanging test (I), and right front limb placing test (J) over time after ICH and DCPIB treatment. Data are presented as box and whisker plots (min to max). B, D, F: One-way ANOVA with Tukey's multiple-comparison test; G-J: two-way ANOVA with Tukey's multiple-comparison test. *p< 0.05, **p< 0.01, ***p< 0.001 vs. ICH + DCPIB (0 mg/kg) (B, D, F) or sham (G-J); #p< 0.05, ##p< 0.01, ###p< 0.001 vs. ICH + DCPIB (10 mg/kg) (B, D, F) or ICH + DCPIB (0 mg/kg) (G-J). Each group contained 5 (B), 8 (D), 9 (F), or 10 (G-J) animals. Scale bars: 100 μm (A, C), 2 mm (E).

swelling under pressure.[22] AMPK is one of the key sensors of metabolic, oxidative, and other stresses[49,50] and currently plays a significant role in regulating phagocytosis.[30,31] In response to stress, intracellular signaling pathways of LRRC8A are activated.[12,51] In line with this notion, blocking LRRC8A caused the activation of AMPK signals in hemin-incubating cells. Although *Lrrc8a* deficiency decreased AMPK activity in muscular cells,[34] we consider that the effect of LRRC8A on AMPK activation may have cell septicity. The mechanism of direct modulation of AMPK by LRRC8A will be a fascinating point to continue exploring LRRC8A regulation of phagocytosis after brain hemorrhage injury in the future.

A recent study showed that astrocytic LRRC8A mediates glutamate release and regulates neuronal excitotoxicity in an ischemic stroke model.[19] Of interest, our findings showed that LRRC8A was expressed in astrocytes that have end-feet on blood vessels, but was rarely present in reactive astrocytes in the perihematomal region after ICH. It is possible that astrocytic LRRC8A channel may participate in regulating blood-brain barrier function and integrity, but not in mediating inflammation-related cytokine/chemokine release under ICH conditions. Consistent with this possibility, knocking down LRRC8A expression in striatal astrocytes and neurons did not improve neurologic function in ICH mice. Although DCPIB is currently widely used as the most potent and preferred LRRC8A/VRAC inhibitor, it has been reported to inhibit H-K-ATPase,[52] inwardly rectifying potassium channels,[53] and two-pore domain potassium (K2P) channels.[54] DCPIB also manipulates glutamate releasing/uptaking by affecting the connexin hemichannel[55] and GLT-1 glutamate transporter protein.[55] Considering the possible off-target effects of DCPIB in enhancing M/Mφ phagocytosis and improving ICH prognosis, we always compared the results gained from DCPIB administration and *Lrrc8a* depletion, and found that they had similar effects on increasing M/Mφ phagocytosis, activating Nrf2/CD36 axis, and correcting neurobehaviors post-ICH. More specific blockers of the LRRC8A/VRAC[56,57] have been discovered, such as SN-401[58] and VI-116.[59] It is worth mentioning that DCPIB and other LRRC8A channel blockers may be administered to acute stroke patients in ambulances in the future, as these drugs are equally effective at improving the prognosis of hemorrhagic and ischemic strokes, possibly through different mechanisms.

A recent study utilized M/Mφ-specific LRRC8A knockout mice and pharmacological inhibition of LRRC8A and demonstrated LRRC8A channel was necessary for cell volume regulation but not involved in the phagocytic activity, cell migration, or p2yr12 dependent chemotaxis of microglia.[21] This is consistent with our result that lack of LRRC8A did not affect the cell phagocytosis mediated by the AMPK-Nrf2-CD36 axis in BV2, microglia, and RAW264.7 cells. However, the inhibitory effect of LRRC8A enhanced the phagocytosis of cells cotreated with hemin. Therefore, we speculate that the regulation of phagocytosis in M/Mφ by LRRC8A requires irritants, such as hemin.

In summary, our findings indicate that inhibition of the LRRC8A channel in M/Mφ significantly reduces perihematomal neuronal death and improves functional recovery after ICH by accelerating hematoma clearance. Mechanistically, eliminating or pharmacologically blocking the LRRC8A channel may promote AMPK activation and Nrf2 nuclear translocation, upregulate *Cd36* expression, and enhance erythrophagocytosis by M/Mφ. These findings not only reveal a new function of the LRRC8A channel in M/Mφ phagocytosis, but also suggest a potential therapeutic target for ICH treatment and M/Mφ phagocytosis-dysfunction related diseases, such as Alzheimer's disease, Parkinson's disease, and infections.

Limitations of the study

The LRRC8A channel can be activated by cell swelling, hypotonicity, and changes in ionic strength.[60] Here, we demonstrated that hemin increases the expression of LRRC8A in M/Mφ. Future studies need to determine whether hemin activates the LRRC8A channel simultaneously and the underlying mechanism. In addition to regulating erythrophagocytosis in M/Mφ, as we have shown, LRRC8A is also involved in other critical physiologic and pathologic processes, including volume regulation, cell proliferation, excitatory amino acid release, cell apoptosis, and cell migration.[14] These effects of LRRC8A depend on the subunit composition (*Lrrc8a-e*) of the LRRC8A channel.[61–64] Although investigating the subunit composition of the LRRC8A channel is beyond the scope of this study, it would be of interest to examine it in future studies.

STAR★METHODS

Detailed methods are provided in the online version of this paper and include the following:

- KEY RESOURCES TABLE

SUPPLEMENTAL INFORMATION

Supplemental information can be found online at https://doi.org/10.1016/j.isci.2022.105527.

ACKNOWLEDGMENTS

The authors thank Claire F. Levine, MS, ELS (Scientific Editor, Department of Anesthesiology and Critical Care Medicine, the Johns Hopkins University), for editing the manuscript. We thank Dr. Zhiqing Xu (Capital Medical University, Beijing) for providing the BV2 cells for the study. Thisword was supported by National Natural Science Foundation of China (81873790 and 32070735 to Q. Li, 81971037 to F. Yang). The Beijing Natural Science Foundation Program and Scientific Research Key Program of Beijing Municipal Commission of Education (KZ202010025033 to Q. Li, KZ201910025026 to F. Yang). The Graphical Abstract was created with BioRender.

AUTHOR CONTRIBUTIONS

L.J. and S.D. are co-first authors. L.J., S.D., W.C., Y.Y., G.Y., X.M., Y.F., and L.Q. designed the experiments and wrote and revised the manuscript. L.J., S.D., W.C., W.W., and L.Z. performed experiments. L.J., S.D., W.C., L.Z. X.Z., P.M., H.T., S.Q., L.M., H.L., D.Y., G.K., and W.X. collected the data; L.J., S.D., W.C., L.Z., W.P., M.Y., T.Y., X.M., Y.F., and L.Q. analyzed the data. All authors have agreed on the final version to be published.

DECLARATION OF INTERESTS

The authors have declared that no conflict of interest exists.

Received: May 9, 2022
Revised: September 26, 2022
Accepted: November 4, 2022
Published: December 22, 2022

REFERENCES

1. Hostettler, I.C., Seiffge, D.J., and Werring, D.J. (2019). Intracerebral hemorrhage: an update on diagnosis and treatment. Expert Rev. Neurother. *19*, 679–694. https://doi.org/10.1080/14737175.2019.1623671.

2. Li, Z., You, M., Long, C., Bi, R., Xu, H., He, Q., and Hu, B. (2020). Hematoma expansion in intracerebral hemorrhage: an update on prediction and treatment. Front. Neurol. *11*, 702. https://doi.org/10.3389/fneur.2020.00702.

3. Wang, G., Wang, L., Sun, X.G., and Tang, J. (2018). Haematoma scavenging in intracerebral haemorrhage: from mechanisms to the clinic. J. Cell Mol. Med. *22*, 768–777. https://doi.org/10.1111/jcmm.13441.

4. Vaibhav, K., Braun, M., Khan, M.B., Fatima, S., Saad, N., Shankar, A., Khan, Z.T., Harris, R.B.S., Yang, Q., Huo, Y., et al. (2018). Remote ischemic post-conditioning promotes hematoma resolution via AMPK-dependent immune regulation. J. Exp. Med. *215*, 2636–2654. https://doi.org/10.1084/jem.20171905.

5. Zhao, X., Aronowski, J., Grotta, J., and Gonzales, N. (2009). Hematoma resolution as a therapeutic target: the role of microglia/macrophages. Stroke *40*, S92–S94. https://doi.org/10.1161/STROKEAHA.108.533158.

6. Gong, Q.W., Liao, M.F., Liu, L., Xiong, X.Y., Zhang, Q., Zhong, Q., Zhou, K., Yang, Y.R., Meng, Z.Y., Gong, C.X., et al. (2017). CD36 gene polymorphisms are associated with intracerebral hemorrhage susceptibility in a han Chinese population. BioMed Res. Int. *2017*, 5352071. https://doi.org/10.1155/2017/5352071.

7. Li, Q., Lan, X., Han, X., Durham, F., Wan, J., Weiland, A., Koehler, R.C., and Wang, J. (2021). Microglia-derived interleukin-10 accelerates post-intracerebral hemorrhage hematoma clearance by regulating CD36. Brain Behav. Immun. *94*, 437–457. https://doi.org/10.1016/j.bbi.2021.02.001.

8. Chang, C.F., Massey, J., Osherov, A., Angenendt da Costa, L.H., and Sansing, L.H. (2020). Bexarotene enhances macrophage erythrophagocytosis and hematoma clearance in experimental intracerebral hemorrhage. Stroke *51*, 612–618. https://doi.org/10.1161/STROKEAHA.119.027037.

9. Oppi, S., Nusser-Stein, S., Blyszczuk, P., Wang, X., Jomard, A., Marzolla, V., Yang, K., Velagapudi, S., Ward, L.J., Yuan, X.M., et al. (2020). Macrophage NCOR1 protects from atherosclerosis by repressing a pro-atherogenic PPARgamma signature. Eur. Heart J. *41*, 995–1005. https://doi.org/10.1093/eurheartj/ehz667.

10. Zhuang, J., Peng, Y., Gu, C., Chen, H., Lin, Z., Zhou, H., Wu, X., Li, J., Yu, X., Cao, Y., et al. (2021). Wogonin accelerates hematoma clearance and improves neurological outcome via the PPAR-gamma pathway after intracerebral hemorrhage. Transl. Stroke Res. *12*, 660–675. https://doi.org/10.1007/s12975-020-00842-9.

11. Röszer, T. (2017). Transcriptional control of apoptotic cell clearance by macrophage nuclear receptors. Apoptosis *22*, 284–294. https://doi.org/10.1007/s10495-016-1310-x.

12. Voss, F.K., Ullrich, F., Münch, J., Lazarow, K., Lutter, D., Mah, N., Andrade-Navarro, M.A., von Kries, J.P., Stauber, T., and Jentsch, T.J. (2014). Identification of LRRC8 heteromers as an essential component of the volume-regulated anion channel VRAC. Science *344*, 634–638. https://doi.org/10.1126/science.1252826.

13. Qiu, Z., Dubin, A.E., Mathur, J., Tu, B., Reddy, K., Miraglia, L.J., Reinhardt, J., Orth, A.P., and Patapoutian, A. (2014). SWELL1, a plasma membrane protein, is an essential component of volume-regulated anion channel. Cell *157*, 447–458. https://doi.org/10.1016/j.cell.2014.03.024.

14. Osei-Owusu, J., Yang, J., Vitery, M.D.C., and Qiu, Z. (2018). Molecular biology and physiology of volume-regulated anion channel (VRAC). Curr. Top. Membr. *81*, 177–203. https://doi.org/10.1016/bs.ctm.2018.07.005.

15. Elorza-Vidal, X., Gaitán-Peñas, H., and Estévez, R. (2019). Chloride channels in astrocytes: structure, roles in brain homeostasis and implications in disease. Int. J. Mol. Sci. *20*, E1034. https://doi.org/10.3390/ijms20051034.

16. Wilson, C.S., and Mongin, A.A. (2018). Cell volume control in healthy brain and neuropathologies. Curr. Top. Membr. *81*, 385–455. https://doi.org/10.1016/bs.ctm.2018.07.006.

17. Law, R.O. (1994). Regulation of mammalian brain cell volume. J. Exp. Zool. *268*, 90–96. https://doi.org/10.1002/jez.1402680204.

18. Kimelberg, H.K., Cragoe, E.J., Jr., Nelson, L.R., Popp, A.J., Szarowski, D., Rose, J.W., Woltersdorf, O.W., Jr., and Pietruszkiewicz, A.M. (1987). Improved recovery from a traumatic-hypoxic brain injury in cats by intracisternal injection of an anion transport inhibitor. Cent. Nerv Syst. Trauma *4*, 3–14. https://doi.org/10.1089/cns.1987.4.3.

19. Yang, J., Vitery, M.D.C., Chen, J., Osei-Owusu, J., Chu, J., and Qiu, Z. (2019). Glutamate-releasing SWELL1 channel in astrocytes modulates synaptic transmission and promotes brain damage in stroke. Neuron *102*, 813–827.e6. https://doi.org/10.1016/j.neuron.2019.03.029.

20. Zhou, J.J., Luo, Y., Chen, S.R., Shao, J.Y., Sah, R., and Pan, H.L. (2020). LRRC8A-dependent volume-regulated anion channels contribute to ischemia-induced brain injury and glutamatergic input to hippocampal neurons. Exp. Neurol. *332*, 113391. https://doi.org/10.1016/j.expneurol.2020.113391.

21. Cook, J.R., Gray, A.L., Lemarchand, E., Schiessl, I., Green, J.P., Newland, M.C., Dyer, D.P., Brough, D., and Lawrence, C.B. (2022). LRRC8A is dispensable for a variety of microglial functions and response to acute stroke. Glia *70*, 1068–1083. https://doi.org/10.1002/glia.24156.

22. Green, J.P., Swanton, T., Morris, L.V., El-Sharkawy, L.Y., Cook, J., Yu, S., Beswick, J., Adamson, A.D., Humphreys, N.E., Bryce, R., et al. (2020). LRRC8A is essential for hypotonicity-but not for DAMP-induced NLRP3 inflammasome activation. Elife *9*, e59704. https://doi.org/10.7554/eLife.59704.

23. Samaranch, L., Salegio, E.A., San Sebastian, W., Kells, A.P., Foust, K.D., Bringas, J.R., Lamarre, C., Forsayeth, J., Kaspar, B.K., and Bankiewicz, K.S. (2012). Adeno-associated virus serotype 9 transduction in the central nervous system of nonhuman primates. Hum. Gene Ther. *23*, 382–389. https://doi.org/10.1089/hum.2011.200.

24. Nieuwenhuis, B., Haenzi, B., Hilton, S., Carnicer-Lombarte, A., Hobo, B., Verhaagen, J., and Fawcett, J.W. (2021). Optimization of adeno-associated viral vector-mediated transduction of the corticospinal tract: comparison of four promoters. Gene Ther. *28*, 56–74. https://doi.org/10.1038/s41434-020-0169-1.

25. Zhou, C., Chen, X., Planells-Cases, R., Chu, J., Wang, L., Cao, L., Li, Z., López-Cayuqueo, K.I., Xie, Y., Ye, S., et al. (2020). Transfer of cGAMP into bystander cells via LRRC8 volume-regulated anion channels augments STING-mediated interferon responses and anti-viral immunity. Immunity *52*, 767–781.e6. https://doi.org/10.1016/j.immuni.2020.03.016.

26. Lahey, L.J., Mardjuki, R.E., Wen, X., Hess, G.T., Ritchie, C., Carozza, J.A., Böhnert, V., Maduke, M., Bassik, M.C., and Li, L. (2020). LRRC8A:C/E heteromeric channels are ubiquitous transporters of cGAMP. Mol. Cell *80*, 578–591.e5. https://doi.org/10.1016/j.molcel.2020.10.021.

27. Kimura, Y., Yanagida, T., Onda, A., Tsukui, D., Hosoyamada, M., and Kono, H. (2020). Soluble uric acid promotes atherosclerosis via AMPK (AMP-Activated protein kinase)-mediated inflammation. Arterioscler. Thromb. Vasc. Biol. *40*, 570–582. https://doi.org/10.1161/ATVBAHA.119.313224.

28. O'Neill, L.A.J., and Hardie, D.G. (2013). Metabolism of inflammation limited by AMPK and pseudo-starvation. Nature *493*, 346–355. https://doi.org/10.1038/nature11862.

29. Herzig, S., and Shaw, R.J. (2018). AMPK: guardian of metabolism and mitochondrial homeostasis. Nat. Rev. Mol. Cell Biol. *19*, 121–135. https://doi.org/10.1038/nrm.2017.95.

30. Bae, H.B., Zmijewski, J.W., Deshane, J.S., Tadie, J.M., Chaplin, D.D., Takashima, S., and Abraham, E. (2011). AMP-activated protein kinase enhances the phagocytic ability of macrophages and neutrophils. Faseb. J. *25*, 4358–4368. https://doi.org/10.1096/fj.11-190587.

31. He, Z., Mao, F., Lin, Y., Li, J., Zhang, X., Zhang, Y., Xiang, Z., Noor, Z., Zhang, Y., and Yu, Z. (2019). Molecular characteristics of AMPK and its role in regulating the phagocytosis of oyster hemocytes. Fish Shellfish Immunol. *93*,

416–427. https://doi.org/10.1016/j.fsi.2019.07.075.

32. Joo, M.S., Kim, W.D., Lee, K.Y., Kim, J.H., Koo, J.H., and Kim, S.G. (2016). AMPK facilitates nuclear accumulation of Nrf2 by phosphorylating at serine 550. Mol. Cell Biol. *36*, 1931–1942. https://doi.org/10.1128/MCB.00118-16.

33. Bewley, M.A., Budd, R.C., Ryan, E., Cole, J., Collini, P., Marshall, J., Kolsum, U., Beech, G., Emes, R.D., Tcherniaeva, I., et al. (2018). Opsonic phagocytosis in chronic obstructive pulmonary disease is enhanced by Nrf2 agonists. Am. J. Respir. Crit. Care Med. *198*, 739–750. https://doi.org/10.1164/rccm.201705-0903OC.

34. Saito, Y., Yako, T., Otsu, W., Nakamura, S., Inoue, Y., Muramatsu, A., Nakagami, Y., Shimazawa, M., and Hara, H. (2020). A triterpenoid Nrf2 activator, RS9, promotes LC3-associated phagocytosis of photoreceptor outer segments in a p62-independent manner. Free Radic. Biol. Med. *152*, 235–247. https://doi.org/10.1016/j.freeradbiomed.2020.03.012.

35. Yu, J., Wang, W.N., Matei, N., Li, X., Pang, J.W., Mo, J., Chen, S.P., Tang, J.P., Yan, M., and Zhang, J.H. (2020). Ezetimibe attenuates oxidative stress and neuroinflammation via the AMPK/Nrf2/TXNIP pathway after MCAO in rats. Oxid. Med. Cell. Longev. *2020*, 4717258. https://doi.org/10.1155/2020/4717258.

36. Mimche, P.N., Thompson, E., Taramelli, D., and Vivas, L. (2012). Curcumin enhances non-opsonic phagocytosis of Plasmodium falciparum through up-regulation of CD36 surface expression on monocytes/macrophages. J. Antimicrob. Chemother. *67*, 1895–1904. https://doi.org/10.1093/jac/dks132.

37. Shaw, P., and Chattopadhyay, A. (2020). Nrf2-ARE signaling in cellular protection: mechanism of action and the regulatory mechanisms. J. Cell. Physiol. *235*, 3119–3130. https://doi.org/10.1002/jcp.29219.

38. Fang, H., Chen, J., Lin, S., Wang, P., Wang, Y., Xiong, X., and Yang, Q. (2014). CD36-mediated hematoma absorption following intracerebral hemorrhage: negative regulation by TLR4 signaling. J. Immunol. *192*, 5984–5992. https://doi.org/10.4049/jimmunol.1400054.

39. Pepino, M.Y., Kuda, O., Samovski, D., and Abumrad, N.A. (2014). Structure-function of CD36 and importance of fatty acid signal transduction in fat metabolism. Annu. Rev. Nutr. *34*, 281–303. https://doi.org/10.1146/annurev-nutr-071812-161220.

40. Lan, X., Han, X., Li, Q., Yang, Q.W., and Wang, J. (2017). Modulators of microglial activation and polarization after intracerebral haemorrhage. Nat. Rev. Neurol. *13*, 420–433. https://doi.org/10.1038/nrneurol.2017.69.

41. Maruyama, A., Tsukamoto, S., Nishikawa, K., Yoshida, A., Harada, N., Motojima, K., Ishii, T., Nakane, A., Yamamoto, M., and Itoh, K. (2008). Nrf2 regulates the alternative first exons of CD36 in macrophages through specific antioxidant response elements. Arch. Biochem. Biophys. *477*, 139–145. https://doi.org/10.1016/j.abb.2008.06.004.

42. Li, Z., Li, M., Shi, S.X., Yao, N., Cheng, X., Guo, A., Zhu, Z., Zhang, X., and Liu, Q. (2020). Brain transforms natural killer cells that exacerbate brain edema after intracerebral hemorrhage. J. Exp. Med. *217*, e20200213. https://doi.org/10.1084/jem.20200213.

43. Audebert, H.J., Schenkel, J., Heuschmann, P.U., Bogdahn, U., and Haberl, R.L.; Telemedic Pilot Project for Integrative Stroke Care Group (2006). Effects of the implementation of a telemedical stroke network: the telemedic pilot project for integrative stroke Care (TEMPiS) in bavaria, Germany. Lancet Neurol. *5*, 742–748. https://doi.org/10.1016/S1474-4422(06)70527-0.

44. Broderick, J.P., Brott, T.G., Duldner, J.E., Tomsick, T., and Huster, G. (1993). Volume of intracerebral hemorrhage. A powerful and easy-to-use predictor of 30-day mortality. Stroke *24*, 987–993. https://doi.org/10.1161/01.str.24.7.987.

45. Hanley, D.F., Thompson, R.E., Rosenblum, M., Yenokyan, G., Lane, K., McBee, N., Mayo, S.W., Bistran-Hall, A.J., Gandhi, D., Mould, W.A., et al. (2019). Efficacy and safety of minimally invasive surgery with thrombolysis in intracerebral haemorrhage evacuation (MISTIE III): a randomised, controlled, open-label, blinded endpoint phase 3 trial. Lancet *393*, 1021–1032. https://doi.org/10.1016/S0140-6736(19)30195-3.

46. Awad, I.A., Polster, S.P., Carrión-Penagos, J., Thompson, R.E., Cao, Y., Stadnik, A., Money, P.L., Fam, M.D., Koskimäki, J., Girard, R., et al. (2019). Surgical performance determines functional outcome benefit in the minimally invasive surgery plus recombinant tissue plasminogen activator for intracerebral hemorrhage evacuation (MISTIE) procedure. Neurosurgery *84*, 1157–1168. https://doi.org/10.1093/neuros/nyz077.

47. Bonsack, F., 4th, Alleyne, C.H., Jr., and Sukumari-Ramesh, S. (2016). Augmented expression of TSPO after intracerebral hemorrhage: a role in inflammation? J. Neuroinflammation *13*, 151. https://doi.org/10.1186/s12974-016-0619-2.

48. Egashira, Y., Hua, Y., Keep, R.F., and Xi, G. (2015). Intercellular cross-talk in intracerebral hemorrhage. Brain Res. *1623*, 97–109. https://doi.org/10.1016/j.brainres.2015.04.003.

49. Garcia, D., and Shaw, R.J. (2017). AMPK: mechanisms of cellular energy sensing and restoration of metabolic balance. Mol. Cell *66*, 789–800. https://doi.org/10.1016/j.molcel.2017.05.032.

50. Song, C., Heping, H., Shen, Y., Jin, S., Li, D., Zhang, A., Ren, X., Wang, K., Zhang, L., Wang, J., and Shi, D. (2020). AMPK/p38/Nrf2 activation as a protective feedback to restrain oxidative stress and inflammation in microglia stimulated with sodium fluoride. Chemosphere *244*, 125495. https://doi.org/10.1016/j.chemosphere.2019.125495.

51. Alghanem, A.F., Abello, J., Maurer, J.M., Kumar, A., Ta, C.M., Gunasekar, S.K., Fatima, U., Kang, C., Xie, L., Adeola, O., et al. (2021). The SWELL1-LRRC8 complex regulates endothelial AKT-eNOS signaling and vascular function. Elife *10*, e61313. https://doi.org/10.7554/eLife.61313.

52. Fujii, T., Takahashi, Y., Takeshima, H., Saitoh, C., Shimizu, T., Takeguchi, N., and Sakai, H. (2015). Inhibition of gastric H+, K+-ATPase by 4-(2-butyl-6, 7-dichloro-2-cyclopentylindan-1-on-5-yl)oxybutyric acid (DCPIB), an inhibitor of volume-regulated anion channel. Eur. J. Pharmacol. *765*, 34–41. https://doi.org/10.1016/j.ejphar.2015.08.011.

53. Deng, W., Mahajan, R., Baumgarten, C.M., and Logothetis, D.E. (2016). The ICl, swell inhibitor DCPIB blocks Kir channels that possess weak affinity for PIP2. Pflügers Archiv *468*, 817–824. https://doi.org/10.1007/s00424-016-1794-9.

54. Lv, J., Liang, Y., Zhang, S., Lan, Q., Xu, Z., Wu, X., Kang, L., Ren, J., Cao, Y., Wu, T., et al. (2019). DCPIB, an inhibitor of volume-regulated anion channels, distinctly modulates K2P channels. ACS Chem. Neurosci. *10*, 2786–2793. https://doi.org/10.1021/acschemneuro.9b00010.

55. Bowens, N.H., Dohare, P., Kuo, Y.H., and Mongin, A.A. (2013). DCPIB, the proposed selective blocker of volume-regulated anion channels, inhibits several glutamate transport pathways in glial cells. Mol. Pharmacol. *83*, 22–32. https://doi.org/10.1124/mol.112.080457.

56. Figueroa, E.E., and Denton, J.S. (2022). A SWELL time to develop the molecular pharmacology of the volume-regulated anion channel (VRAC). Channels *16*, 27–36. https://doi.org/10.1080/19336950.2022.2033511.

57. Maertens, C., Droogmans, G., Chakraborty, P., and Nilius, B. (2001). Inhibition of volume-regulated anion channels in cultured endothelial cells by the anti-oestrogens clomiphene and nafoxidine. Br. J. Pharmacol. *132*, 135–142. https://doi.org/10.1038/sj.bjp.0703786.

58. Gunasekar, S.K., Xie, L., Kumar, A., Hong, J., Chheda, P.R., Kang, C., Kern, D.M., My-Ta, C., Maurer, J., Heebink, J., et al. (2022). Small molecule SWELL1 complex induction improves glycemic control and nonalcoholic fatty liver disease in murine Type 2 diabetes. Nat. Commun. *13*, 784. https://doi.org/10.1038/s41467-022-28435-0.

59. Jeon, D., Ryu, K., Jo, S., Kim, I., and Namkung, W. (2022). VI-116, A novel potent inhibitor of VRAC with minimal effect on ANO1. Int. J. Mol. Sci. *23*, 5168. https://doi.org/10.3390/ijms23095168.

60. Hoffmann, E.K., Lambert, I.H., and Pedersen, S.F. (2009). Physiology of cell volume regulation in vertebrates. Physiol. Rev. *89*, 193–277. https://doi.org/10.1152/physrev.00037.2007.

61. Konishi, T., Shiozaki, A., Kosuga, T., Kudou, M., Shoda, K., Arita, T., Konishi, H., Komatsu, S., Kubota, T., Fujiwara, H., et al. (2019). LRRC8A expression influences growth of esophageal squamous cell carcinoma. Am. J.

Pathol. *189*, 1973–1985. https://doi.org/10.1016/j.ajpath.2019.06.006.

62. Schober, A.L., Wilson, C.S., and Mongin, A.A. (2017). Molecular composition and heterogeneity of the LRRC8-containing swelling-activated osmolyte channels in primary rat astrocytes. J. Physiol. *595*, 6939–6951. https://doi.org/10.1113/JP275053.

63. Planells-Cases, R., Lutter, D., Guyader, C., Gerhards, N.M., Ullrich, F., Elger, D.A., Kucukosmanoglu, A., Xu, G., Voss, F.K., Reincke, S.M., et al. (2015). Subunit composition of VRAC channels determines substrate specificity and cellular resistance to Pt-based anti-cancer drugs. EMBO J. *34*, 2993–3008. https://doi.org/10.15252/embj.201592409.

64. Zahiri, D., Burow, P., Großmann, C., Müller, C.E., Klapperstück, M., and Markwardt, F. (2021). Sphingosine-1-phosphate induces migration of microglial cells via activation of volume-sensitive anion channels, ATP secretion and activation of purinergic receptors. Biochim. Biophys. Acta Mol. Cell Res. *1868*, 118915. https://doi.org/10.1016/j.bbamcr.2020.118915.

65. Li, Q., Han, X., Lan, X., Gao, Y., Wan, J., Durham, F., Cheng, T., Yang, J., Wang, Z., Jiang, C., et al. (2017). Inhibition of neuronal ferroptosis protects hemorrhagic brain. JCI Insight *2*, e90777. https://doi.org/10.1172/jci.insight.90777.

66. Parkhurst, C.N., Yang, G., Ninan, I., Savas, J.N., Yates, J.R., 3rd, Lafaille, J.J., Hempstead, B.L., Littman, D.R., and Gan, W.B. (2013). Microglia promote learning-dependent synapse formation through brain-derived neurotrophic factor. Cell *155*, 1596–1609. https://doi.org/10.1016/j.cell.2013.11.030.

67. Lapchak, P.A., Zhang, J.H., and Noble-Haeusslein, L.J. (2013). RIGOR guidelines: escalating STAIR and STEPS for effective translational research. Transl. Stroke Res. *4*, 279–285. https://doi.org/10.1007/s12975-012-0209-2.

68. MacLellan, C.L., Silasi, G., Poon, C.C., Edmundson, C.L., Buist, R., Peeling, J., and Colbourne, F. (2008). Intracerebral hemorrhage models in rat: comparing collagenase to blood infusion. J. Cerebr. Blood Flow Metabol. *28*, 516–525. https://doi.org/10.1038/sj.jcbfm.9600548.

69. Clark, W., Gunion-Rinker, L., Lessov, N., and Hazel, K. (1998). Citicoline treatment for experimental intracerebral hemorrhage in mice. Stroke *29*, 2136–2140.

70. Zhou, J., Zhuang, J., Li, J., Ooi, E., Bloom, J., Poon, C., Lax, D., Rosenbaum, D.M., and Barone, F.C. (2013). Long-term post-stroke changes include myelin loss, specific deficits in sensory and motor behaviors and complex cognitive impairment detected using active place avoidance. PLoS One *8*, e57503. https://doi.org/10.1371/journal.pone.0057503.

71. Zhu, W., Gao, Y., Chang, C.F., Wan, J.R., Zhu, S.S., and Wang, J. (2014). Mouse models of intracerebral hemorrhage in ventricle, cortex, and hippocampus by injections of autologous blood or collagenase. PLoS One *9*, e97423. https://doi.org/10.1371/journal.pone.0097423.

72. Pu, H., Shi, Y., Zhang, L., Lu, Z., Ye, Q., Leak, R.K., Xu, F., Ma, S., Mu, H., Wei, Z., et al. (2019). Protease-independent action of tissue plasminogen activator in brain plasticity and neurological recovery after ischemic stroke. Proc. Natl. Acad. Sci. USA *116*, 9115–9124. https://doi.org/10.1073/pnas.1821979116.

73. Wang, G., Li, T., Duan, S.N., Dong, L., Sun, X.G., and Xue, F. (2018). PPAR-Gamma promotes hematoma clearance through haptoglobin-hemoglobin-CD163 in a rat model of intracerebral hemorrhage. Behav. Neurol. *2018*, 7646104. https://doi.org/10.1155/2018/7646104.

74. Ikenari, T., Kurata, H., Satoh, T., Hata, Y., and Mori, T. (2020). Evaluation of fluoro-jade C staining: specificity and application to damaged immature neuronal cells in the normal and injured mouse brain. Neuroscience *425*, 146–156. https://doi.org/10.1016/j.neuroscience.2019.11.029.

75. Friard, J., Tauc, M., Cougnon, M., Compan, V., Duranton, C., and Rubera, I. (2017). Comparative effects of chloride channel inhibitors on LRRC8/VRAC-mediated chloride conductance. Front. Pharmacol. *8*, 328. https://doi.org/10.3389/fphar.2017.00328.

76. Xiao, Z., Shen, D., Lan, T., Wei, C., Wu, W., Sun, Q., Luo, Z., Chen, W., Zhang, Y., Hu, L., et al. (2022). Reduction of lactoferrin aggravates neuronal ferroptosis after intracerebral hemorrhagic stroke in hyperglycemic mice. Redox Biol. *50*, 102256. https://doi.org/10.1016/j.redox.2022.102256.

STAR★METHODS

KEY RESOURCES TABLE

REAGENT or RESOURCE	SOURCE	IDENTIFIER
Antibodies		
anti-LRRC8A	Santa Cruz	sc-517113
anti-AMPK	Cell Signaling Technology	Cat# 5832S; RRID: AB_10624867
anti-phospho-AMPK	Cell Signaling Technology	Cat# 50081S; RRID: AB_2799368
anti-Nrf2	Proteintech	Cat# 16396-1-AP; RRID: AB_2782956
anti-lamin B1	Invitrogen	Cat# MA1-06103; RRID: AB_2281281
anti-CD36	Santa Cruz	Cat# sc-7309; RRID: AB_627044
anti-IgA	Abcam	ab37322
Compound C	Abcam	ab120843
anti-α-tubulin	Abcam	Cat# ab52866; RRID: AB_869989
anti-β-actin	Santa Cruz	Cat# sc-47778; RRID: AB_626632
anti-mouse IgG HRP-conjugated secondary antibodies	Cell Signaling Technology	Cat# 7076S; RRID: AB_330924
anti-rabbit IgG HRP-conjugated secondary antibodies	Cell Signaling Technology	Cat# 7074S; RRID: AB_2099233
anti-Iba-1	Wako	Cat# 019–19741; RRID: AB_839504
anti-GFAP	Sigma-Aldrich	Cat# SAB5700611; RRID: AB_2827276
anti-NeuN	Cell Signaling Technology	Cat# 12943; RRID: AB_2630395
Goat anti-Mouse IgG (H + L) Highly Cross-Adsorbed Secondary Antibody, Alexa Fluor™ Plus 488	Invitrogen	Cat# A32723; RRID: AB_2633275
Donkey anti-Rabbit IgG (H + L) Highly Cross-Adsorbed Secondary Antibody, Alexa Fluor™ Plus 594	Invitrogen	Cat# A32754; RRID: AB_2762827
Bacterial and virus strains		
AAV9-CMV-mCherry-U6-Lrrc8a shRNA	ObiO Technology	N/A
Scrambled AAV9-CMV-mCherry-U6-scramble shRNA	ObiO Technology	N/A
Mouse lentivirus Lrrc8a shRNA	ObiO Technology	N/A
Scrambled mouse lentivirus Lrrc8a shRNA	ObiO Technology	N/A
Chemicals, peptides, and recombinant proteins		
TRIzol reagent	Invitrogen	15596018
DMEM/F12	Gibco	11039021
Penicillin/streptomycin	Sigma-Aldrich	V900929
DAPI	Cell Signaling Technology	4083S
DCPIB	Tocris	1540/10
Hemin	Frontier Scientific	7084–24–4
ML385	Selleck	S8790
RIPA Lysis buffer	Boster	AR0101
30% sodium hydroxide	Beijing Dingguo Changsheng Biotechnology	94000101
Potassium permanganate	Sinopharm	10017318
Fluoro Jade C (FJC) staining solution	Millipore	AG325

(*Continued on next page*)

Continued

REAGENT or RESOURCE	SOURCE	IDENTIFIER
Xylene	Sinopharm	1330–20–7
Ethanol	Sinopharm	64–17–5
Luxol Fast Blue	Sigma-Aldrich	S3382
Lithium carbonate	Sigma-Aldrich	62470
CV	Sigma-Aldrich	C5042
PowerUpTM SYBRTM Green Master Mix	Applied Biosystems	A25742
TGF-β2	Peprotech	100-35-10UG
IL-34	MCE	HY-P73212
PKH26	Sigma-Aldrich	MKCM1863
α-MEM	KeyGEN BioTECH	KGM119900-1
M-CSF	Peprotech	AF-315-02
Percoll	Solarbio	P8370
Calcein red-AM	BioLegend	425205
Bovine serum albumin	BIOBYING	9048–46–8
Triton X-100	Sigma-Aldrich	123K0112
Tamoxifen	Sigma-Aldrich	T5648
Corn oil	Macklin	C805618
Critical commercial assays		
Phagocytic assay	Invitrogen	P35361
Hemoglobin assay kit	Sigma-Aldrich	MAK115
Reverse transcriptase kit	Vazyme	R323–01
DNA gel extraction kit	Qiagen	Cat. No. 28706X4
BCA protein assay kit	Thermo	23,221
The Mouse Phagocytosis Pathway RT2 Profiler PCR array	Qiagen	Cat No. 330231
Experimental models: Cell lines		
BV2	Provided from Dr. Zhiqing Xu (Capital Medical University, Beijing)	N/A
RAW 264.7	Procell Life Science & Technology Co., Ltd., Wuhan, China	N/A
Experimental models: Organisms/strains		
C57BL/6 mice	Vital River Laboratories	N/A
Adult Lrrc8a$^{fl/fl}$; Cx3cr1$^{creERT/+}$ mice	Vital River Laboratories	N/A
littermate Lrrc8a$^{fl/fl}$ mice	Vital River Laboratories	N/A
Lrrc8a$^{fl/fl}$	Vital River Laboratories	N/A
Software and algorithms		
ImageJ	NIH Image	Fiji, 2.1.0/1.53c
GraphPad Prism 8	GraphPad	www.graphpad.com

RESOURCE AVAILABILITY

Lead contact

(qianli@ccmu.edu.cn).

Materials availability

This study did not generate new unique reagents.

Data and code availability

- The PCR array data are listed in Table S1 as supplementary information. The original western blot images have been shown in the supplemental information.
- This paper does not report the original code.
- Any additional information required to reanalyze the data reported in this paper is available from the lead contact upon request.

EXPERIMENTAL MODEL AND SUBJECT DETAILS

Experimental design

Animals that died or had a neurological deficit score higher than 20 at 24 h after surgery were euthanized and excluded from the analysis. A power analysis based on our previous studies[65] and pilot data indicated that eight mice/group would provide at least 80% power for detecting a 20% decrease in neurologic deficit at $\alpha = 0.05$ (two-sided) in neurobehavior tests. The animals and cell cultures for each group were randomized. Treatment, data collection, and data analyses were blinded by using different investigators or by masking the sample labels.

For *in vitro* experiments, we added 20 μM hemin (7084–24–4, Frontier Scientific, USA) and/or 20 μM DCPIB (1540/10, Tocris, USA) to BV2, RAW 264.7, primary macrophages and microglia for 6 h. We treated cells with 5 μM ML385 (S8790, Selleck, USA), 10 μM Compound C (ab120843, Abcam, USA), anti-IgA (1:500, ab37322, Abcam), or anti-CD36 (1:500, ab23680, Abcam) 2 h before hemin and/or DCPIB exposure.

For *in vivo* experiments, 10 or 30 mg/kg DCPIB or vehicle was administered daily by intra-peritoneal injection to wildtype mice for 3 days beginning 2 h after ICH. Vehicle, 50 μM ML385, 100 μM compound C, anti-IgA (1:50), or anti-CD36 (1:50) was injected into the ipsilateral lateral ventricle of *Lrrc8a* conditional knockout (cKO) mice just before ICH.

Animals and ethics

Male WT mice (C57BL/6 mice, 6–8 weeks old) were obtained from Vital River Laboratories (Beijing, China). To generate *Lrrc8a* cKO mice that lack *Lrrc8a* in M/Mφ, $Lrrc8a^{fl/fl}$ and $Cx3cr1^{creERT}$ mice (C57BL/6 background) were obtained from the Shanghai Model Organisms Center (Shanghai, China) and crossed.[66] The animals were bred and housed under specific-pathogen-free conditions at the Capital Medical University (Beijing, China), and housed in a regulated environment (22 ± 2°C, 55 ± 5% humidity) with a 12-h light: dark cycle (lights on at 8:00 am). Mice received a standard diet and had unrestricted access to food and water.

To generate the $Lrrc8a^{fl/fl}$ mice, we microinjected Cas9 mRNA, gRNA, and the donor vector into fertilized eggs of WT mice. The sequences used have been listed in Tables S2 and S3. Tamoxifen (150 mg/kg body weight; 20 mg/mL stock solution; T5648, Sigma-Aldrich, USA) dissolved in corn oil (C805618, Macklin, China) was administered once daily for 5 consecutive days by intra-peritoneal injection to $Lrrc8a^{fl/fl}$; $Cx3cr1^{creERT}$ mice to activate the creERT recombination or littermates $Lrrc8a^{fl/fl}$ mice as control mice before use. Age- and sex-matched littermates or WT mice were administered equivalent doses of tamoxifen and used as controls. No developmental issues were noticed in all mouse strains used in this study.

Experiments of animals were performed and reported according to the ARRIVE and ICLAS guidelines.[67] During the treatment period, no adverse effects were observed in the mice. In all experiments, adequate measures were taken to minimize any discomfort or distress. All procedures were approved by the Experimental Animal Ethics Committee of Capital Medical University. Anesthesia and euthanasia of animals were consulted with the American Veterinary Medical Association Guidelines for the Euthanasia of Animals (2020). Mice between treatment groups were sibling matched and all WT, $Lrrc8a^{fl/fl}$ and $Lrrc8a^{fl/fl}$; $Cx3cr1^{creERT}$ mice used for the experiments were male mice, and 6 to 8-week-old adult mice were used in most experiments unless otherwise as indicated. Exact value for each group *n* and the total number of each experiment are reported (including any independent replicates). Online randomnumber generators (https://www.graphpad.com/quickcalcs/randomize1/) was used to randomly group experimental animals. We have consistently implemented blinding during allocation, the conduct of the experiment, the outcome assessment and the data analysis to minimize these subjective biases.

Cell lines

BV2 cells (a gift from Dr. Zhiqing Xu group) and mouse primary microglia which were isolated from p0-1 pups were cultured in DMEM/F12 medium (11320033, Gibco, USA) supplemented with 10% fetal bovine serum (FBS, 16140071, Gibco). RAW 264.7 cells (Procell Life Science & Technology Co., Ltd., Wuhan, China) were cultured in RPMI1640 medium (A4192301, Gibco) supplemented with 10% FBS.

METHOD DETAILS

ICH models

Mice were anesthetized by inhaling 1–3% isoflurane and ventilated with oxygen-enriched air as 20%:80%. For the blood injection ICH model, 35 μL of autologous blood drawn from the tail were infused into the left striatum (x = 2.0 mm, y = −0.8 mm, z1 = 3.10 mm; z2 = 3.22 mm) at a speed of 0.5 μL/min. For the collagenase injection model, 0.5 μL of 0.075 U collagenase VII-S (C2399, Sigma-Aldrich) was infused (x = 2.0 mm, y = −0.8 mm, z = 3.22 mm) at a speed of 0.1 μL/min. The sham-operated control mice received only needle insertion.[65,68]

Behavioral tests

All behavioral tests were evaluated and analyzed by an observer blinded to group on different recovery days after the onset of ICH. A 24-point neurological deficit scoring system, which included body symmetry, gait, climbing, circling behavior, front limb symmetry, and compulsory circling was used to evaluate neurologic function.[69] Each test score ranged from 0 to 4 based on mild to severe performance, with a total score of 24. For the hindlimb placing test,[70,71] the mice were placed on the edge of a table, and the contralateral hind limbs were gently pulled below the edge of the table. If the limbs were quickly retracted and placed on the edge of the table accurately, a score of 0 was given; delayed pullback was scored 1 point; no retraction of the limbs was scored 2 points. The total score out of 10 trials was recorded for each mouse. The wire hanging test was used to evaluate grip strength and motor performance.[72] The mice were placed on the middle of an iron wire (2 mm in diameter, 50 cm in length) between two platforms 50 cm above the ground. Padding was placed beneath to cushion falls. Mice were scored as follows: fall = 0, hanging onto wire with forelimbs = 1, hanging on and attempting to climb onto the wire = 2, hanging onto wire with more than three limbs = 3, climbing onto the wire with four limbs and tail but failing to reach platform = 4, and successfully climbing onto either platform = 5. The duration of each test was 30 s. The test was repeated four times for each mouse, and the scores of the last three trials were averaged to determine the performance. Forelimb placing was assessed with a vibrissae-elicited forelimb placing test. The mouse was placed on the edge of a tabletop, and the vibrissae on one side were brushed. Intact animals placed the contralateral forelimb quickly on the tabletop. Placing was quantified as the percentage of successful responses in 10 trials.

Analysis of hematoma volume and hemoglobin content

The mice were euthanized by deep anesthesia, and coronal brain sections (1 mm thick) were cut with a mouse brain slice mold (40–75, RWD). The sections were digitized and analyzed with ImageJ (Fiji, 2.1.0/1.53c, NIH Image, USA). We photographed all brain sections of each mouse for quantification. The total volume of hematoma was calculated and used for statistical analysis.

The hemoglobin content was measured with a hemoglobin assay kit (MAK115, Sigma-Aldrich) according to the manufacturer's instructions.[73] Briefly, 4-mm thick brain tissue from the ipsilateral striatum, including the hematoma core and perihematomal region, was collected and homogenized for 3 min by sonication in 300 μL of ice-cold phosphate-buffered saline (PBS). After the homogenate was centrifuged, 50 μL of the supernatant was mixed with 200 μL hemoglobin detection reagent. The mixture was incubated for 5minat room temperature, and the absorbance was measured at 400 nm. The optical density of each sample was plotted on a standard curve.

Fluoro-Jade C staining

Brains were cut to a thickness of 16 μm and placed on slides in series. Brain sections were immersed in 1% sodium hydroxide (94000101, Beijing Dingguo Changsheng Biotechnology, China) in 80% and 70% ethanol (64–17–5, Sinopharm, China) and distilled water. Then the slides were incubated in 0.06% potassium permanganate (10017318, Sinopharm) and rinsed with distilled water. Finally, the slides were incubated for 20 min in 0.0004% fluoro Jade C (FJC) staining solution (AG325, Millipore, USA), which selectively binds

to degenerating neurons.[74] After being rinsed and cleared with xylene (1330–20–7, Sinopharm), the sections were observed and photographed under a fluorescence microscope (Eclipse Ti-U, Nikon, Japan) at an excitation wavelength of 450–490 nm. We photographed at least nine locations per mouse in the perihematomal region [3 fields (upper, left, and right) per section × 3 sections (bregma 1.70 mm, 0.74 mm, and −0.46 mm)] for quantification. The mean value of the nine fields was calculated and used for statistical analysis. Positively stained cells were counted manually by an investigator blinded to group.

Luxol Fast Blue/Cresyl violet double staining

Luxol Fast Blue/Cresyl violet (CV) double staining was used to quantify the lesion volume.[65] Briefly, the brain sections in series (16-μm-thick) were mounted on slides, immersed in 70% ethanol for 24 h and 0.1% Luxol Fast Blue staining solution (S3382, Sigma-Aldrich, USA) at 56°C overnight. The sections were rinsed with PBS and decolorized in 0.05% lithium carbonate solution (62470, Sigma-Aldrich). Then, the sections were counterstained with 0.2% CV (C5042, Sigma-Aldrich) and dehydrated by a serial increased concentration of ethanol. The slides were immersed in xylene and mounting medium and then observed under a light microscope (Eclipse Ci, Nikon). ImageJ software was used to quantify the lesion volume was calculated. We photographed all brain sections of each mouse at an interval of 96 μm for quantification. The total volume of hematoma was calculated and used for statistical analysis. When comes to CV staining, at least twelve locations per mouse in the perihematomal region [4 fields (upper, lower, left, and right) per section × 3 sections (bregma 1.70 mm, 0.74 mm, and −0.46 mm)] for quantification. The mean value of the twelve fields was calculated and used for statistical analysis.

Quantitative real-time RT-PCR

Total RNA from the ipsilateral striatum or treated cells was extracted using TRIzol reagent (15596018, Invitrogen, USA). Approximately 800 ng of RNA from each sample was reverse-transcribed to cDNA using a reverse transcriptase kit (R323–01, Vazyme, China). Then, real-time PCR was carried out in a 7500 Fast Real-Time PCR System (Applied Biosystems, USA) using the PowerUpTM SYBRTM Green Master Mix (A25742, Applied Biosystems). Gene expression was normalized to that of GAPDH. The real-time PCR primers used are listed in Table S4.

Viral infection

The adeno-associated virus AAV9-CMV-mCherry-U6-*Lrrc8a* shRNA (8.4 + 1012 V.G./mL), scrambled AAV9-CMV-mCherry-U6-scramble shRNA (7.4 + 1012 V.G./mL), mouse lentivirus *Lrrc8a* shRNA, and vector shRNA were purchased from ObiO Technology (China). BV2 cells were infected with lentivirus (MOI = 100) for 12hat 50–60% confluence.

Primary microglia culture

Adult $Lrrc8a^{fl/fl}$; $Cx3cr1^{creETR+/-}$ or $Lrrc8a^{fl/fl}$ mice were perfused using iced PBS, with skulls immersed in alcohol, and brains were collected in Hanks' solution, and olfactory bulb and brainstem were removed. Brains were minced with Papain and DNAse digestions for 30 min. Cells digestion was terminated with DMEM/F12 (Gibco) supplemented with 10% FBS, 1% penicillin/streptomycin (Sigma). Following termination, a Pasteur pipette was used to dissociate the brain into a single-cell suspension. The cells were centrifuged at 4°C 500 g for 5 min after sieving, resuspended in FBS, and then given 30% Percoll (P8370, Solarbio, China) at 4°C 800 g for 15 min to remove the myelin. After resuspension of cells with MACS buffer (PBS, 0.5% BSA, 2 mM EDTA) and counting, incubated anti-CD11b antibody magnetic beads (Miltenyi) on a roller for 15 min. We performed a quadroMACS separator with LS columns (Miltenyi) according to the manufacturer's instructions to enrich the microglia. After counting, 1.5×10^4 cells were spot-plated onto 96-well Cell+ plates (Corning, USA) or 6×10^4 cells confocal plates (Corning, USA). Cells were cultured in DMEM/F12 (Gibco) supplemented with 10% FBS (Gibco), 2 mM glutamine, 1% penicillin/streptomycin (Sigma), 50 ng/mL TGF-β2 (Peprotech, 100-35-10UG, USA) and 20 ng/mL IL-34 (HY-P73212, MCE, USA) for 7 days.

BMDM culture

Bone marrow-derived macrophages were flushed from the tibia and femurs of 8-week-old mice and cultured in α-MEM (KGM119900-1, KeyGEN BioTECH, China) supplemented with 10% FBS, 1% penicillin/streptomycin (Sigma) and 20 ng/mL mouse M-CSF (AF-315-02, Peprotech, USA) for 7 days.

Regulatory volume decrease assay

Raw 264.7 were cultured in DMEM/F12 (Gibco) supplemented with 10% FBS (Gibco), 1% penicillin/streptomycin (Sigma), and transfected with mouse lentivirus Lrrc8a shRNA or scrambled shRNA (MOI = 100) for 12 h. RAW264.7 cells (32 × 10^4) were spot-plated onto black 96-well Cell+ plates (3603, Corning) and cultured in RPMI1640 medium supplemented with 10% FBS for 48 h. 10 uM calcein red-AM (BioLegend, 425205) was stained for 1h, washed three times with medium, and left for 30min. Use isotonic buffer (132 mM NaCl, 2.5 mM KCl, 2 mM $CaCl_2$, 2 mM $MgCl_2$, 10 mM Glucose, 20 mM HEPES, pH 7.4, 312 mOsm/L) washed cells three times. Calcein fluorescence was detected using a microplate reader with a fluorescence capturing function (SpectraMax iD5, USA). Readings were taken every 2 min, and hypotonic stimuli induce at 5 min by adding distilled water (isotonic buffer: distilled water = 7:3, (218 mOsm/kg). The ratio of the fluorescence intensity of each well at different times to the fluorescence intensity of the first assay was calculated as yielding F/F0 curves. The area under the statistical curve values of the curves were analyzed in Prism as reported previously.[75]

PCR array for mouse phagocytosis

The Mouse Phagocytosis Pathway RT2 Profiler PCR array was purchased from Qiagen (GeneGlobe ID-PAMM-173ZC, Catalog No. 330231) and used for quantitative PCR in the ABI 7500 Fast Block system (Applied Biosystems, USA).[76] The data were uploaded for analysis to the Qiagen website (http://www.qiagen.com/geneglobe). The data were calculated as fold change/regulation using the ΔΔCT method, in which delta CT is calculated between gene of interest and an average of reference genes, followed by ΔΔCT calculations [ΔCT (Test Group) − ΔCT (Control Group)]. Fold change is then calculated using the $2^{-\Delta\Delta CT}$ formula. The data analysis web portal plotted a clustergram and heat map, and the report was exported from the Qiagen web portal at GeneGlobe. Variations in gene expression between BV2 cells treated with hemin + vehicle and those treated with hemin + DCPIB are shown as fold increase or decrease.

Chromatin immunoprecipitation (ChIP) assay

BV2 cells were incubated for 6 h with 20 μM hemin and 20 μM DCPIB. Then, after being incubated with 1% formaldehyde for 1 h, they were collected by centrifugation. Chromatin was disrupted by sonication in lysis buffer on ice for 5 min in cycles of 30 s on and 30 s off. The protein-DNA complex was incubated with Nrf2 antibodies (1:200, CST, 12721) overnight at 4°C and then blocked with protein G beads for 2hat 4°C with shaking. The rabbit IgG antibody was used as a negative control. The immunocomplexes were washed with low-salt buffer, high-salt buffer, LiCl buffer, and TE buffer sequentially for 10 min each at 4°C. The immunoprecipitated antibody-protein-DNA complexes were eluted with elution buffer and heated in a 65°C water bath for 6 h. DNA was purified with the DNA gel extraction kit (Qiagen, Valencia, CA), eluted with distilled water, and used for quantitative Real-time RT-PCR analysis (the primers used are listed in Table S4). PCR products were separated by gel electrophoresis on 2% agarose gels.

Phagocytic assay

Phagocytosis was quantified by using the pHrodo™ Red BioParticles® Conjugates for Phagocytosis (P35361, Invitrogen). After cells incubated with the BioParticles® suspension for 20 min, the phagocytic capacity was measured on a spectrophotometer (SpectraMax iD5, Molecular DEVICES).

For the erythrophagocytosis assay, RBCs from WT mice were extracted and stained with PKH26 (MKCM1863, Sigma-Aldrich) according to the manufacturer's protocol. Then, RBCs were added to the macrophages at a ratio of 10:1 and incubated at 37°C for 30 min. Non-phagocytosed RBCs were washed with PBS. Macrophages were stained with Iba-1. Nuclei were stained with DAPI. Cells were observed with a confocal microscope (TCS SP8 STED, Leica, Germany). Images were taken at 63× magnification under an oil immersion lens. ImageJ was used for the quantification of phagocytosed RBCs.

Cytoplasmic and nuclear extraction

Six-well plates were washed with 1 mL of PBS per well for BV2 cells. Centrifuge the cell suspension at 6000 rpm for 2 min and discard the supernatant and collect the cell precipitate. Add 50 uL of buffer A (with protease inhibitor before use) and leave to lyse on ice for 8 min, followed by centrifugation at 1300*g* for 5 min at 4°C and collect the supernatant. The supernatant was centrifuged at 20,000 g for 15minat 4°C, and the supernatant was the cytoplasmic protein, and the precipitate was reserved for the extraction

of cytosolic protein. The cytoplasmic proteins were quantified in concentration according to Western blot experiment. β-actin was used as an internal control.

The precipitate was washed with buffer A and centrifuged at 1300 g for 5minat 4°C. 24 uL of RIPA (with 1% SDS) was added to the precipitate to lyse the nucleoproteins. Add 6 uL of 5× loading buffer, heat at 95°C for 20 min in a metal bath, centrifuge at 4°C for 15minat 12,000 g, collect the supernatant and discard the precipitate. The next step is to perform protein electrophoresis according to the Western blot procedure. Laminin B1 was used as an internal control.

Western blot analysis

The ipsilateral striatum of the mouse brain and cultured cells were homogenized in enhanced RIPA lysis buffer (AR0101, Boster, China) and 10% protease inhibitor cocktail (04693132001, Roche, USA) by sonication. The protein concentration was determined with the BCA protein assay kit (23221, Thermo). The proteins were separated by sodium dodecyl sulfate-polyacrylamide gel electrophoresis and transferred onto polyvinylidene difluoride membranes (1620177, Bio-Rad, USA), which were blocked in 5% non-fat milk before being incubated with primary antibodies overnight at 4°C. The primary antibodies were anti-LRRC8A (sc-517113, Santa Cruz, USA), anti-AMPK (5832S, Cell Signaling Technology, USA), anti-phospho-AMPK (Thr172; 50081S, Cell Signaling Technology, USA), anti-Nrf2 (16396-1-AP, Proteintech, USA), anti-lamin B1 (MA1-06103, Invitrogen), anti-CD36 (sc-7309, Santa Cruz), anti-α-tubulin (ab52866, Abcam), and anti-β-actin (sc-47778, Santa Cruz). The membranes were washed with TBST buffer and then incubated with IgG HRP-conjugated secondary antibodies (anti-mouse, 7076S, Cell Signaling Technology, or anti-rabbit, 7074S, Cell Signaling Technology) for 1h at room temperature. Immunoreactive bands were visualized by using chemiluminescent HRP substrate (90719, Millipore, USA). The bands were scanned and analyzed with ImageJ software.

Immunofluorescence staining

The mice were perfused with iced PBS (pH 7.4) and 4% PFA. The brain was post-fixed in 4% PFA at 4°C overnight, cryoprotected in 30% sucrose for 48 h, and then cut into 16-μm serial sections. The sections were blocked in 10% goat serum, 1% bovine serum albumin (9048–46–8, BIOBYING, China), and 0.5% Triton X-100 (123K0112, Sigma-Aldrich) in PBS. Then they were incubated with primary antibody overnight at 4°C. The primary antibodies were against LRRC8A (sc-517113, Santa Cruz), Iba-1 (019–19741, Wako), GFAP (SAB5700611, Sigma-Aldrich), and NeuN (12943, Cell Signaling Technology). The sections were then washed in PBS and incubated with secondary antibodies (A32723/A32754, Invitrogen) conjugated to fluorophores according to the staining. Nuclei were stained with DAPI. Images of brain sections were captured under a confocal microscope (TCS SP8 STED, Leica, Germany) with an oil immersion lens at 63× magnification. ImageJ was used for the quantification of mean fluorescence intensity and cell number. We photographed at least nine locations per mouse in the perihematomal region [3 fields (upper, left, and right) per section × 3 sections] for quantification. The mean value of the nine fields was calculated and used for statistical analysis. Positively stained cells were counted manually by an investigator blinded to group.

QUANTIFICATION AND STATISTICAL ANALYSIS

Data are presented as mean ± SD with dot plots or bar graphs. We compared two groups using a two-tailed Student's *t* test followed by Welch's correction. We evaluated group comparisons of all behavioral tests by one-way or two-way ANOVA followed by Tukey's or Sidak's *post-hoc* test. $p < 0.05$ was considered a statistically significant difference.